OXFORD

Human Molecular Genetics, 2015, Vol. 24, No. 24 6958–6974

doi: 10.1093/hmg/ddv399
Advance Access Publication Date: 24 September 2015
Original Article

ORIGINAL ARTICLE

Disruption of murine *Adamtsl4* results in zonular fiber detachment from the lens and in retinal pigment epithelium dedifferentiation

Gayle B. Collin[1,†], Dirk Hubmacher[2,†], Jeremy R. Charette[1,†], Wanda L. Hicks[1], Lisa Stone[1], Minzhong Yu[3,4], Jürgen K. Naggert[1], Mark P. Krebs[1], Neal S. Peachey[3,4,5], Suneel S. Apte[2,‡] and Patsy M. Nishina[1,*,‡]

[1]The Jackson Laboratory, Bar Harbor, ME, USA, [2]Department of Biomedical Engineering, Cleveland Clinic Lerner Research Institute, Cleveland, OH, USA, [3]Cole Eye Institute, Cleveland Clinic, Cleveland, OH, USA, [4]Department of Ophthalmology, Cleveland Clinic Lerner College of Medicine of Case Western Reserve University, Cleveland, OH, USA and [5]Louis Stokes Cleveland VA Medical Center, Cleveland, OH, USA

*To whom correspondence should be addressed at: The Jackson Laboratory, 600 Main Street, Bar Harbor, ME 04609, USA. Tel: +1 2072886383; Fax: +1 2072886077; Email: patsy.nishina@jax.org

Abstract

Human gene mutations have revealed that a significant number of ADAMTS (a disintegrin-like and metalloproteinase (reprolysin type) with thrombospondin type 1 motifs) proteins are necessary for normal ocular development and eye function. Mutations in human *ADAMTSL4*, encoding an ADAMTS-like protein which has been implicated in fibrillin microfibril biogenesis, cause ectopia lentis (EL) and EL et pupillae. Here, we report the first ADAMTSL4 mouse model, *tvrm267*, bearing a nonsense mutation in *Adamtsl4*. Homozygous *Adamtsl4*^{tvrm267} mice recapitulate the EL phenotype observed in humans, and our analysis strongly suggests that ADAMTSL4 is required for stable anchorage of zonule fibers to the lens capsule. Unexpectedly, homozygous *Adamtsl4*^{tvrm267} mice exhibit focal retinal pigment epithelium (RPE) defects primarily in the inferior eye. RPE dedifferentiation was indicated by reduced pigmentation, altered cellular morphology and a reduction in RPE-specific transcripts. Finally, as with a subset of patients with *ADAMTSL4* mutations, increased axial length, relative to age-matched controls, was observed and was associated with the severity of the RPE phenotype. In summary, the *Adamtsl4*^{tvrm267} model provides a valuable tool to further elucidate the molecular basis of zonule formation, the pathophysiology of EL and ADAMTSL4 function in the maintenance of the RPE.

Introduction

As in most organs, tissues of the eye contain an extracellular matrix (ECM), which provides structural scaffolding for cells, regulates fluid and macromolecular transport, modulates cell signaling and influences cellular processes such as differentiation, proliferation, migration and adhesion. The ECM comprises an organized, hierarchical network built from proteins and polysaccharides, and varies according to location, cell type and organ system (1). Major components of the ECM typically include fibrous proteins, such as collagens, elastin, fibronectin, laminins and fibrillins, as well as proteoglycans (1). The ECM is continuously remodeled in response to internal and environmental

---

[†]The authors wish it to be known that, in their opinion, the first three authors should be regarded as joint First Authors.

[‡]The authors wish it to be known that, in their opinion, the last two authors should be regarded as joint Last Authors.

Received: June 16, 2015. **Revised:** August 25, 2015. **Accepted:** September 21, 2015

cues and the balance between synthesis and degradation of ECM molecules is tightly regulated. Even subtle ECM dysregulation can induce profound changes in the structure and function of tissues, and, therefore, is a major pathological mechanism underlying many diseases including ocular conditions (1,2).

An emerging class of proteins important in ECM homeostasis are the ADAMTS (*a* *d*isintegrin-like *a*nd *m*etalloproteinase (reprolysin type) with *t*hrombo*s*pondin type 1 motifs) proteins, a superfamily containing 19 ADAMTS proteases and seven ADAMTS-like proteins (ADAMTSL) (3,4). ADAMTS proteases contain a zinc-binding metalloprotease domain and an ancillary domain containing thrombospondin type 1 repeats (TSRs), whereas ADAMTSL proteins lack a protease domain, and consequently, are not proteolytic enzymes.

However, despite the lack of proteolytic activity, ADAMTSL proteins play an important role in the ECM, as exemplified by the diseases that occur when they are disrupted. For example, in humans, recessive *ADAMTSL4* mutations lead to isolated ectopia lentis (EL; MIM# 225100) (5,6), EL et pupillae (MIM# 225200) (7), craniosynostosis with EL (8,9), congenital abnormalities of the iris, and refractive errors that may lead to amblyopia and early-onset cataract (10). Occasional increased intraocular pressure and retinal detachment have also been attributed to *ADAMTSL4* mutations (6,10). Additionally, the axial length of eyes is increased in some patients with *ADAMTSL4* mutations (5,11). *In vitro*, ADAMTSL4 has been characterized as a secreted glycoprotein deposited in the ECM (12). ADAMTSL4 co-localizes with fibrillin-1 microfibrils and enhances fibrillin-1 microfibril deposition in the ECM of cultured fibroblasts (12). Fibrillin microfibrils are sometimes referred to as oxytalan fibers, based on their retention of aldehyde-fuchsin stain following prior oxidation (13,14). They are the principal component of the ocular zonule, a cell-free rigging that suspends the lens in the optic path which mediates accommodation and is disrupted in EL (15–18).

In this study, we report the first mouse model of *Adamtsl4* deficiency, which was generated by *N*-ethyl-*N*-nitrosourea (ENU) mutagenesis on a C57BL/6J (B6) background in the Translational Vision Research Models (TVRM) program at The Jackson Laboratory (19). The *tvrm267* mutants bear a nonsense point mutation in the *Adamtsl4* gene, resulting in a premature stop codon at amino acid position 609. Homozygous *Adamtsl4*^{tvrm267} mice develop EL, which we demonstrate is due to a defect in the anchoring of zonule fibers to the lens surface and is likely related to the strong *Adamtsl4* expression in lens epithelium. Unexpectedly, we observe a variably severe focal and regional dedifferentiation of the retinal pigment epithelium (RPE) with functional deficits. We also find increased axial length, relative to controls, in eyes with a severe RPE phenotype. These defects are investigated here in detail and provide new insights on how *ADAMTSL4* mutations may lead to eye disease similar to that found in humans.

Results

Adamtsl4 is mutated in *tvrm267* mice

The *tvrm267* locus was mapped to mouse Chromosome 3 using a DNA pooling strategy and subsequently localized to an ∼13 Mbp region between markers *D3Mit40* and *D3Mit11* (20). Analysis of high-throughput sequence data in the minimal region revealed a nonsense mutation in *Adamtsl4* (Fig. 1A), resulting from a single

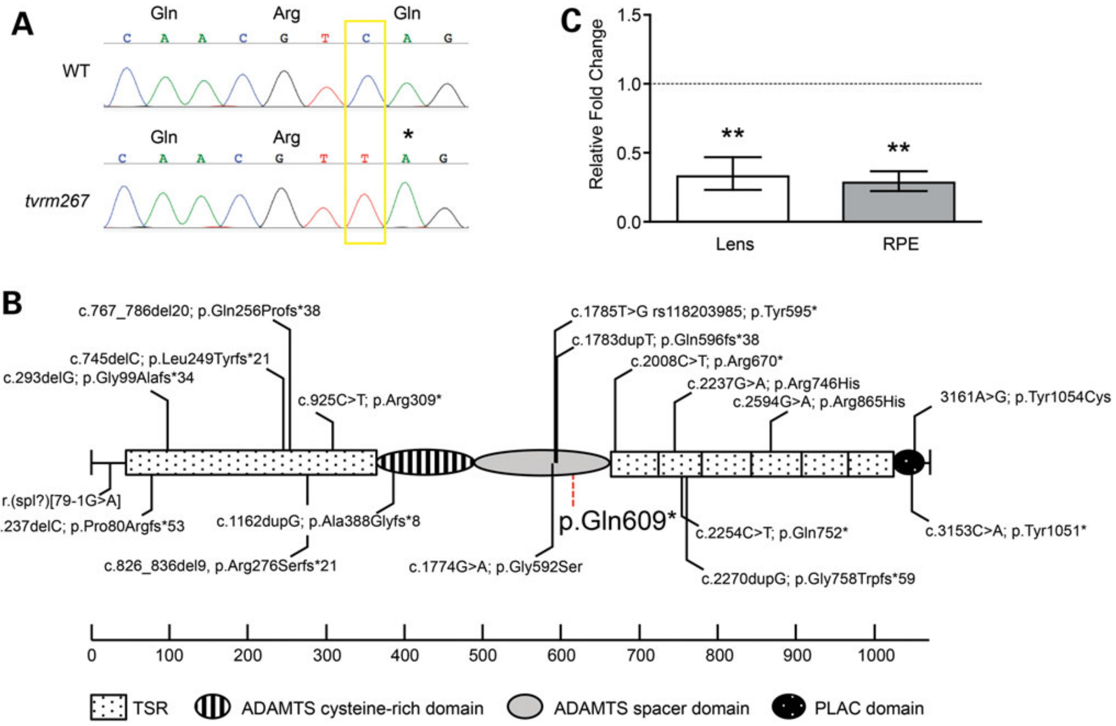

Figure 1. Genetic and molecular analysis of the *tvrm267* mutation. (**A**) By Sanger sequence analysis, a single base pair transition mutation was observed from C>T at nucleotide 1825 of the *Adamtsl4* gene (GenBank, NM_001301705). This mutation is predicted to replace the glutamine (Gln) codon at amino acid position 609 with an early termination codon (p.Gln609*). (**B**) Schematic describing the location of the mutation in *Adamtsl4*^{tvrm267} and *ADAMTSL4* mutations found in human patients (5–9,21–24). The specific domains of ADAMTSL4 are illustrated. TSR1 is unusually long because of a large insertion present only in ADAMTSL4 and ADAMTSL6. (**C**) Nonsense-mediated decay is suggested by comparison of quantitative RT–PCR of mutant and WT control lens and RPE *Adamtsl4* mRNA. Error bars reflect propagating error as defined in the Materials and Methods section. **$P < 0.01$ ($n = 4$).

nucleotide change in exon 11 (c.1825C>T), predicted to replace a glutamine (Gln) codon at amino acid position 609 of the polypeptide with a termination codon (p.Gln609*). This mutation cosegregated with the ‘splatter’ phenotype (described below) in the mapping cross. All other nucleotide changes in the high-throughput sequence data, within the critical region, were either synonymous single nucleotide polymorphisms (SNPs) in exons of genes or occurred in intergenic or intronic regions that were partially covered in the exome capture library. The *Adamtsl4*^{tvrm267} mutation is located near the C-terminal end of the spacer module (Fig. 1B). This mutation has not been previously reported among the several known human mutations, which are distributed throughout the protein (Fig. 1B). Quantitative real-time (qRT)-PCR of lens and RPE-enriched RNA indicated a significant fold change of 0.328 and 0.285 relative to controls, respectively, corresponding to a 3.0- to 3.5-fold decrease of *Adamtsl4* mRNA expression in homozygous mutant mice. This result suggests that *Adamtsl4*^{tvrm267} transcripts may undergo nonsense-mediated mRNA decay, a typical consequence of premature stop codons that do not involve the final coding exon (Fig. 1C) (25).

Adamtsl4 mRNA is strongly expressed in the equatorial lens epithelium, which is the insertion site of the ciliary zonule, as well as in other regions of the eye including the RPE

In humans, ADAMTSL4 was localized to the iris, ciliary body, ciliary processes, RPE and choroid by immunostaining (12,26). Neuroretinal expression of *ADAMTSL4* is debated. Because the available antibodies do not cross-react with mouse ADAMTSL4, we performed *in situ* hybridization (ISH) using RNAscope to precisely identify the cell types expressing *Adamtsl4* mRNA. As shown by ISH of wild-type (WT) eyes, *Adamtsl4* is strongly expressed in the lens epithelium at the lens equator throughout embryonic development and in adults (Fig. 2A). The lens capsule of the equatorial region is one insertion site for the ciliary zonule (15,18); the other is the inner limiting membrane of the ciliary body, which secretes the fibrillins that form the ciliary zonule (17,27). *Adamtsl4* expression was not detected in the ciliary body. At 6 months of age, *Adamtsl4* mRNA expression was detectable (Fig. 2A), but was much reduced compared with the earlier time points examined. A negative control with the bacterial *dapB* probe gave no signal (Fig. 2B). In other parts of the anterior segment of the eye, *Adamtsl4* expression was low in comparison with the lens epithelium; however, we detected expression in the developing corneal stroma and the corneal epithelium at embryonic day 16.5 (e.16.5), postnatal day (P) 21 and 6 months of age (Fig. 2C), and in the pupillary and ciliary zone of the iris at P0 and P21 (Fig. 2D). In the posterior segment, we detected *Adamtsl4* expression in the RPE at P0 and P21 (Fig. 2E). In summary, *Adamtsl4* mRNA was strongly expressed in the equatorial lens epithelium and was present, albeit at markedly lower levels in other tissues of the anterior and posterior segments of the eye.

Adamtsl4^{tvrm267} homozygous mutants recapitulate the EL phenotype observed in human patients

To determine whether eyes from homozygous *Adamtsl4*^{tvrm267} mice develop EL, we examined eyes between birth and 6 months of age by oxytalan fiber staining (Fig. 3A), a histochemical

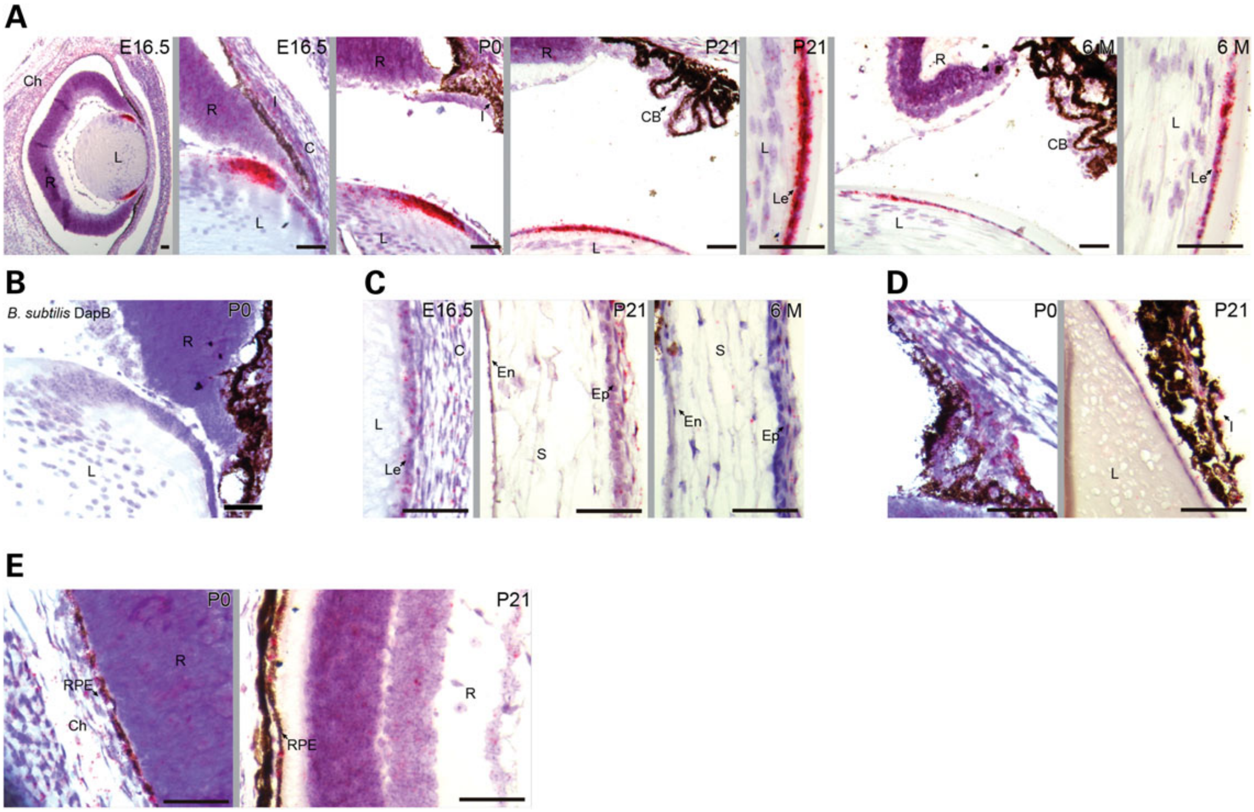

Figure 2. *Adamtsl4* mRNA localization in eyes of WT mice. (**A**) *Adamtsl4* mRNA (indicated by red dots overlying cells) is strongly expressed at the lens equator throughout development of the eye. (**B**) No signal was observed using the bacterial *dapB* probe. (**C** and **D**) *Adamtsl4* expression was detected in the corneal stroma and epithelium (C) and in the pupillary and ciliary zone of the iris (D). (**E**) *Adamtsl4* is expressed in the developing choroid and RPE. C, cornea; CB, ciliary body; Ch, choroid; En, corneal endothelium; Ep, corneal epithelium; I, iris; L, lens; Le, lens epithelium; R, retina; RPE, retinal pigment epithelium, S; corneal stroma. Scale bars: 50 µm.

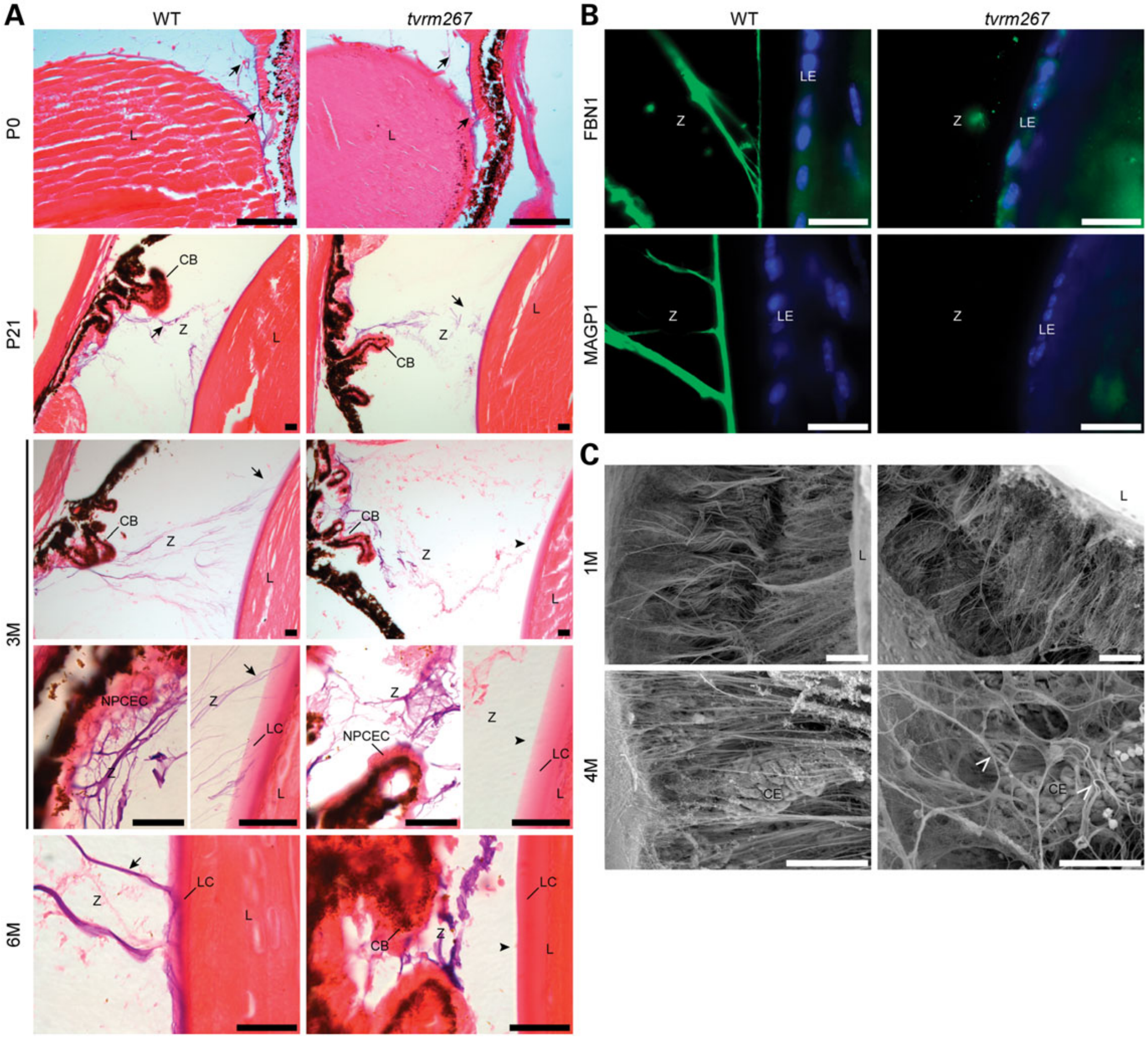

Figure 3. Ciliary zonules are formed, but detach from the lens capsule as the mutants age. (**A**) Oxytalan staining (blue-violet color) of fibrillin microfibrils (arrows) in the ciliary zonule (Z) of sections from WT and *Adamtsl4*^{tvrm267} mutant mice at postnatal day (P) 0 and P21 and at 3 and 6 months (3 M, 6 M) of age. Both WT and *Adamtsl4*^{tvrm267} mutant mice have a normal zonule composition at birth (P0) and at P21 (arrows). While at 3 and 6 months of age, the zonule fibers arise from the ciliary body (CB) in both the WT and the *Adamtsl4*^{tvrm267} mutant eyes, oxytalan fibers in mutant mice do not insert in the lens epithelium (arrowheads) as observed in WT mice (arrows). Sections in (A) were counterstained with eosin. CB, ciliary body; L, lens; LC, lens capsule; LE, lens epithelium; NPCEC, non-pigmented ciliary epithelial cells; Z, zonule. (**B**) Immunostaining with antibodies against FBN1 and MAGP1 (*green*) indicates that zonule fibers are absent in the lens capsule. Cell nuclei were counterstained with DAPI (*blue*). (**C**) Scanning electron micrograph of the ciliary body, posterior zonule and posterior lens showing the normal structure of zonule fibers in control and mutants at 1 month of age. At 4 months of age, the posterior zonule fibers are disorganized (arrowhead) in *Adamtsl4*^{tvrm267} mice compared with age-matched controls. (*n* = 3–4 mice per genotype) R, retina; L, lens; V, vitreous; Z, zonule; LE, lens epithelium; CE, ciliary epithelium. Scale bars: (A–C) 20 µm; (D) 50 µm.

staining method used to visualize elastin-free fibrillin microfibrils. At birth (P0) and at 3 weeks of age (P21), continuity of the zonule, i.e. from the ciliary body to the lens, was observed in both WT and homozygous mutants. In contrast, at 3 months of age, zonule continuity at its lens insertion was lost in homozygous *Adamtsl4*^{tvrm267} mutant eyes, suggesting that the disruption occurred during the juvenile period between 3 weeks and 3 months of age. At 6 months of age, *Adamtsl4*^{tvrm267} mutants lacked the zonule attachment to the lens, including the fibers normally present in the WT lens capsule. However, oxytalan fibers were present in the zonule region and were attached to the inner limiting membrane overlaying the non-pigmented ciliary epithelium of the ciliary body.

Immunostaining of eyes with antibodies to fibrillin-1 (FBN1) and microfibril-associated glycoprotein 1 (MAGP1/MFAP2) showed that 6-month-old *Adamtsl4*^{tvrm267} homozygous mutant eyes contained microfibrils in the vicinity of the ciliary body, but not the lens (Fig. 3B). These microfibrils stained strongly with fibrillin-1 and MAGP1, as expected, and comparably to WT eyes, but were discontinuous from the ciliary body to lens capsule. As expected in the mouse eye, fibrillin-2 (FBN2) zonule staining (17) was also observed (not shown). In WT mouse eyes, we consistently observed fibrillin-1 and MAGP1 staining overlapping with the lens capsule, which was absent in the homozygous *Adamtsl4*^{tvrm267} mutant mice. Other than this difference, the composition of zonule microfibrils, ascertained by FBN1, FBN2 and

MAGP1 staining, did not differ during the juvenile period (Fig. 3B), and staining of the lens capsule with antibodies to collagen IV and laminin or periodic acid-Schiff's reagent failed to disclose differences between the WT and mutants (data not shown).

Scanning electron microscopy of eyes at 1 and 4 months of age (Fig. 3C) revealed an intact zonule at 1 month of age in mutant eyes (also shown in Fig. 3A). However, in 4-month-old mutant mice, i.e. after EL was observed, zonular fibers extending from the ciliary epithelium were markedly disorganized, as might be expected after detachment from the lens. Taken together, these data demonstrate that ADAMTSL4 is necessary for maintaining the molecular interactions that connect zonular fibers to the lens capsule.

Adamtsl4^{tvrm267} mutants develop focal and regional RPE defects

Fundus examination of homozygous *Adamtsl4*^{tvrm267} mice by indirect ophthalmoscopy revealed bright focal lesions of various sizes surrounding the posterior pole (Fig. 4A–D). We termed this phenotype 'splatter', as it is reminiscent of light colored paint thrown against a dark canvas. The lesions lacked the characteristic raised appearance of pathologic structures observed in mouse models of retinal dysplasia (28), suggesting that alterations to the RPE might be involved. In bright field images of the central fundus, B6 (WT control) mice showed normal structure with few spots (Fig. 4A and B), whereas *Adamtsl4*^{tvrm267} mutant mice exhibited a robust splatter phenotype with a regional distribution surrounding the posterior pole and extending toward the inferior fundus (Fig. 4C). Close examination of the fundus images suggested a reduction or complete loss of pigmentation in RPE cells associated with the focal lesions (Fig. 4D).

To assess the cellular basis of the splatter phenotype, we stained RPE flat mounts of *Adamtsl4*^{tvrm267} mice with rhodamine-conjugated phalloidin to detect filamentous actin (F-actin) and DAPI to reveal nuclei. In contrast to WT RPE (Fig. 4E and F), which exhibited a typical polygonal array of nucleated cells, mutant mice showed nucleated cells with greatly reduced apical F-actin, observed individually or in contiguous patches of two or more cells (Fig. 4G and H). These patches corresponded precisely with the sharply delimited lesions observed by bright field fundus imaging, indicating that both apical F-actin and pigmentation are reduced in lesions (compare Fig. 4D and G showing the same field of view). The projected area of cells within patches was larger than in unaffected regions, suggesting that these cells are comparatively flattened, and these cells were characteristically elongated as shown by Feret diameter analysis (Fig. 4I).

Although all mice homozygous for the *Adamtsl4*^{tvrm267} mutation ultimately showed the splatter phenotype in at least one eye, variation in severity between eyes and among homozygous mutants was observed (Fig. 4J and K). Analysis of *Adamtsl4*^{tvrm267} mutants with a grading scheme (Supplementary Material, Fig. S1) indicated that the phenotype was absent at 1 month of age, but progressed rapidly between 1 and 3 months and more slowly thereafter, until ~40% of the population had the highly affected bilateral phenotype by 10 months of age (Fig. 4L). These results suggested that the splatter phenotype arose as a result of a postnatal process that progressed rapidly during the juvenile period.

As fundus imaging was limited to roughly 1/8th of the entire posterior eye in mutant mice, lesion distribution was also examined in image mosaics of entire RPE flat mounts. This analysis confirmed the regional prevalence of lesions associated with the splatter phenotype within a central area surrounding the optic nerve head (Fig. 4M) and extending with a statistically significant bias toward the inferior fundus (Supplementary Material, Fig. S2).

H&E-stained cross-sections through the retina revealed regions in which RPE cells were severely thinned and depigmented relative to controls (Fig. 5A–C). These areas likely correspond to the patches observed in fundus images and flat mounts. Additionally, larger areas of hypopigmentation often appeared adjacent to areas of hyperpigmentation (Fig. 5C). The thickness of the outer nuclear layer (ONL) appeared to be only slightly reduced relative to controls at 12 months of age (Fig. 5A and B). Ectopic, pigmented cells were often found directly adjacent to the apical surface of the RPE (Fig. 5B and C). Ultrastructural examination revealed that the size and distribution of the electron dense granules in these ectopic cells was similar to those found in the underlying RPE (Fig. 5D). Additionally, amorphous material was observed sub-retinally.

Evidence for RPE dedifferentiation in *Adamtsl4*^{tvrm267} mutants

F-actin staining revealed focal distortion of cell morphology as well as RPE cell shedding structures (Fig. 4G and H; Supplementary Material, Fig. S3). To further assess whether the RPE cells were undergoing changes in cell morphology that often are observed during dedifferentiation (29), we immunostained retinal sections with anti-ezrin, an apical marker expressed in fully differentiated RPE cells (30). While continuous ezrin staining was found along the apical RPE of control mice, intermittent staining of apical RPE was observed in *Adamtsl4*^{tvrm267} mice, indicating a potential loss of apical processes (Fig. 6A). We further examined the ultrastructure of the RPE by transmission electron microscopy (Fig. 6B–D). In areas of thinned RPE from *Adamtsl4*^{tvrm267} mutants, we observed disorganized regions along the apical border with areas lacking apical processes (Fig. 6B). In addition, we identified cells devoid of the basal infoldings that are typically uniformly organized adjacent to Bruch's membrane (Fig. 6B–D). Together with evidence for decreased pigmentation and loss of apical F-actin, the reduction of apical ezrin and the absence of apical processes and basal infoldings in thinned cells suggest a cellular reorganization consistent with RPE cell dedifferentiation.

Dedifferentiation of RPE cells leads to downregulation of RPE-specific gene expression and a significant increase in *Col18a1* in *Adamtsl4*^{tvrm267} homozygotes

Expression levels of *Rpe65*, *Rgr* and *Lrat*, which are predominantly expressed in differentiated RPE cells (31), were compared at 1, 3 and 6 months of age in mutants and age-matched controls by qRT–PCR. At 1 month, mutant mice do not exhibit the splatter phenotype; at 3 months, lesions begin to appear; and at 6 months, most mice exhibit the phenotype (see Fig. 4L). The retinas of the particular cohort of mutant mice used for the RT–PCR analysis were mildly affected at 6 months. Expression levels of these genes in mutants did not differ from controls at 1 and 3 months but were reduced by ~20% at 6 months of age (Fig. 7A). To determine whether RPE genes encoding proteins important in tight junctions, basement membranes (BMs) and ECM formation were similarly affected, enriched RPE preparations of 6-month-old WT and *Adamtsl4*^{tvrm267} mice were tested. In this cohort, mutant mice exhibited a severe splatter phenotype. We confirmed that the RPE-specific genes, *Lrat*, *Rgr* and *Rpe65* were significantly down-regulated in mutant mice when compared with WT controls, but interestingly, the reduction ranged from 40 to 50% of

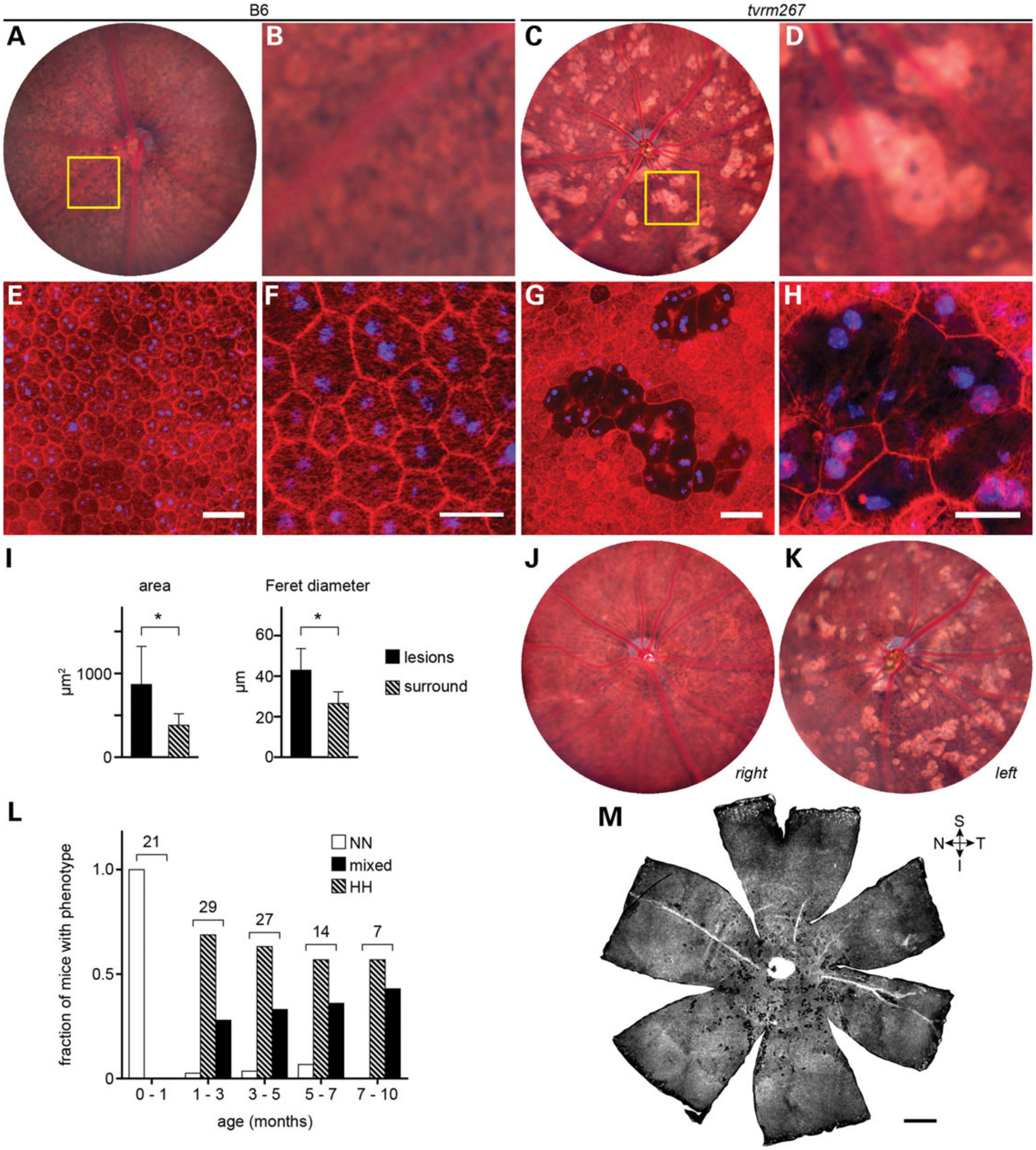

Figure 4. *Adamtsl4*^{tvrm267} mice develop RPE lesions. (**A**) Bright field fundus image of a WT (B6) mouse at 3 months of age. (**B**) Detail of boxed area in (A) showing the normal appearance of the RPE. (**C**) Bright lesions, consistent with hypopigmentation, in a 3-month-old *Adamtsl4*^{tvrm267} mutant. (**D**) Detail of boxed area in (C) showing an alteration in pigmentation among RPE cells associated with bright lesions. (**E–H**) Fluorescence micrographs of RPE flatmounts stained for F-actin (rhodamine phalloidin, *red*) and nuclei (DAPI, *blue*). (E) WT flatmount showing the normal polygonal architecture of the RPE as revealed by F-actin staining at cell boundaries. (F) Detail of panel (E) showing mono- and binucleated cells, and phalloidin staining within cell boundaries due to F-actin in apical processes. (G) Flatmount of the homozygous *Adamtsl4*^{tvrm267} eye shown in panels (C) and (D) indicating a precise correspondence of the lesions. (H) Detail of panel (G) showing that in areas associated with lesions, many cells are enlarged and have diminished phalloidin staining ($n = 3$). (**I**) Morphometric analysis of *Adamtsl4*^{tvrm267} mice at 3 months of age indicating an increase in area and Feret diameter of RPE cells within lesions. Cells within lesions ($n = 55$) were compared with cells in the area surrounding the lesions ($n = 372$). Asterisks: $P < 0.0001$; error bars indicate mean ± SD. (**J** and **K**) Fundus images (J, right eye; K, left eye) showing the variability in lesion severity within an individual homozygous *Adamtsl4*^{tvrm267} mouse. (**L**) Incidence of RPE lesions with age. The splatter phenotype was graded in homozygous *Adamtsl4*^{tvrm267} eyes by indirect ophthalmoscopic evaluation (severity of phenotype: N, none; L, low; M, medium; H, high; see grading scale in Supplementary Material, Fig. S1). The number of mice with a grade in both eyes of no (NN) or high (HH), or any other combination (mixed) was determined in ranges up to ~10 months of age. The total number of mice examined within each age range is indicated. Mice were free of lesions up to 1 month of age. The fraction with a mixed or bilateral high splatter phenotype increased dramatically between 1 and 3 months and progressed slowly thereafter. (**M**) Whole flatmount from a homozygous *Adamtsl4*^{tvrm267} eye showing a regional distribution of lesions in the mutant near the optic nerve head with a bias toward the inferior fundus. Quadrants are designated S, superior; I, inferior; T, temporal; N, nasal. B6 controls: (A, B, E and F); *tvrm267* mutants: (C, D, G, H, J, K, M). Scale bars: (E and G) 50 µm; (F and H) 25 µm; (M) 500 µm.

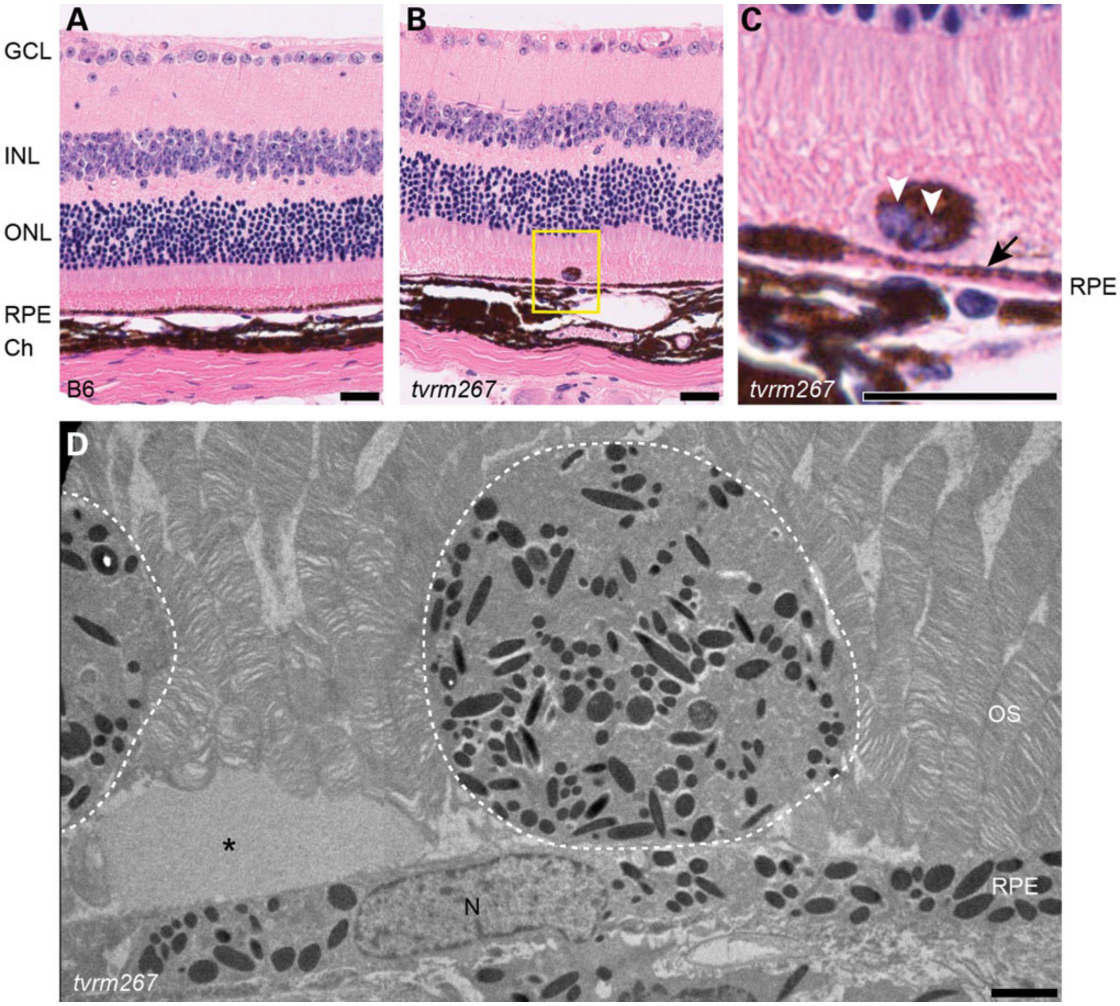

Figure 5. Areas of RPE thinning and subretinal ectopic pigmented cells are observed in *Adamtsl4*^{tvrm267} mice. (**A**) H&E staining of methanol/acetic acid fixed sections shows RPE of uniform thickness in a 1-year-old WT (B6) mouse. (**B**) Age-matched mutant mice exhibit variable RPE thickness as well as perturbations to the outer retina. (**C**) Closer view of the H&E stained section (yellow box) showing thinning of RPE (arrow) and an ectopic binucleated (white arrowheads) pigmented cell adjacent to the thinned area. (**D**) Electron micrograph of subretinal ectopic pigments observed in *Adamtsl4*^{tvrm267} mice. Dashed lines highlight the cells rich in electron dense granules. Asterisk indicates amorphous material. GCL, ganglion cell layer; INL, inner nuclear layer; ONL, outer nuclear layer; RPE, retinal pigmented epithelium; Ch, Choroid; OS, outer segment; N, nucleus. Scale bars: (A–C) 25 µm; (D) 2 µm.

control values, corresponding to the phenotypic severity of the disease (Fig. 7B). *Cdh2* and *Fbn1* expression levels were also reduced in mutants relative to controls, whereas *Col18a1* was increased 5-fold compared with controls.

The *Adamtsl4*^{tvrm267} mutant allele does not affect pupil position but significantly increases axial length in affected eyes

Mutations in *ADAMTSL4* in human patients have been associated with aberrant pupil positioning (7) and increased axial length (5,11). We examined *Adamtsl4*^{tvrm267} mice for mis-positioned pupils by slit lamp biomicroscopy. As shown in Figure 8A, pupils of homozygous *Adamtsl4*^{tvrm267} mutants were centered and not shaped differently compared with the WT littermates.

For axial length determination, we realized that the variable presentation of the splatter phenotype meant it was necessary to identify affected eyes prior to measuring axial length. Therefore, an indirect ophthalmoscopy grading scheme of lesion severity (Supplementary Material, Fig. S1) was used to segregate eyes that were severely affected (Fig. 4K) from those that were unaffected or only slightly affected (Fig. 4J). No difference in axial length was observed at 1 month of age, when none of the mice examined showed lesions (Fig. 8B). However, at 9 months of age, a significant increase in axial length of 4.8% was observed in splatter-affected *Adamtsl4*^{tvrm267} mutants compared with unaffected or slightly affected eyes, which exhibited a similar axial length as eyes from heterozygous or WT mice (Fig. 8B). In addition, homozygous *Adamtsl4*^{tvrm267} mice presented with a combined phenotype that includes EL and an increase in axial length, consistent with the phenotype observed in patients with mutations in *ADAMTSL4*, as well as RPE defects.

RPE functional defects in homozygous *Adamtsl4*^{tvrm267} mice

We examined outer neural retinal and RPE function using strobe flash and dc-ERG protocols, respectively (32). At each age examined, the strobe flash responses of *Adamtsl4*^{tvrm267} mutants had a normal waveform under both dark- and light-adapted

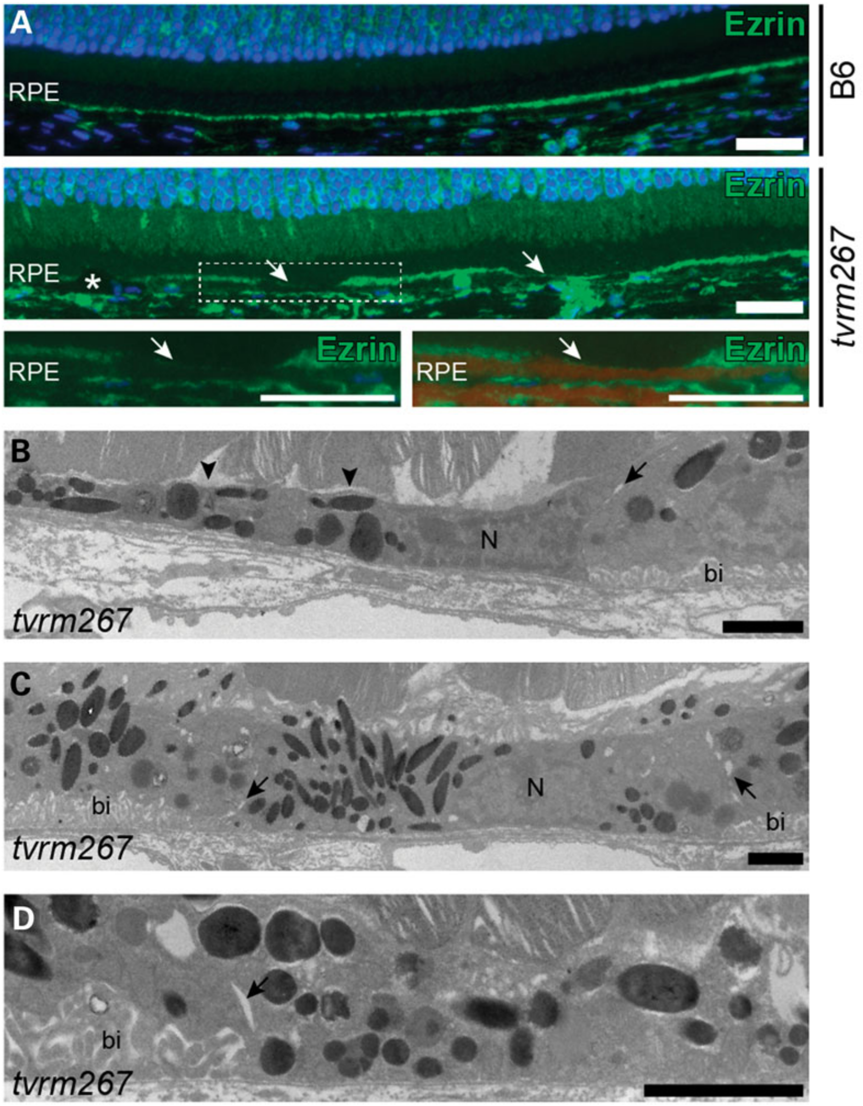

Figure 6. Apical and basolateral aberrations in *Adamtsl4*^{tvrm267} mice. (**A**) Ezrin (*green*) immunostaining in the RPE of 4-month-old control (B6) and mutant mice. Arrows show areas with decreased levels of ezrin in *Adamtsl4*^{tvrm267} RPE. Asterisk indicates an ectopic, pigmented cell. *Lower panels*: (*left*) Image of boxed area (white) shown at higher magnification. (*right*) Overlay of the corresponding brightfield image with the ezrin-stained image shows areas with decrease ezrin levels that are on apical side of the RPE pigment (*dark red*). (**B–D**) TEM images of RPE from a 5-month-old *Adamtsl4*^{tvrm267} mouse show some cells with normal basal infoldings (bi) in the basolateral region, while adjacent cells lack basal infoldings. Junctions of cells lacking basal infoldings are indicated by arrows. Areas devoid of apical processes are also shown (arrowheads). N, nucleus. Scale bars: (A) 25 µm; (B–D) 2 µm.

conditions. Consistent with the anatomic preservation of the ONL, the major response components had comparable amplitudes in 6-month-old *Adamtsl4*^{tvrm267} mutants when compared with *Adamtsl4*$^{tvrm267/+}$ and WT littermates (Fig. 9A and B). When we examined ERG components generated by the RPE, however, we noted that response amplitudes were significantly reduced in 6-month-old homozygous *Adamtsl4*^{tvrm267} mutants while responses of *Adamtsl4*$^{tvrm267/+}$ heterozygotes were comparable with those of WT littermates (Fig. 9C and D). To determine whether this phenotype was age-dependent, we also examined younger mice. As summarized in Figure 9E, a modest reduction in a-wave amplitude was observed in homozygous *Adamtsl4*^{tvrm267} mutants at all ages, which did not change from 1 to 6 months of age. Similar results were obtained for the ERG b-wave recorded under both dark- and light-adapted conditions (data not shown). In comparison, while there was no difference in c-wave amplitudes of homozygous *Adamtsl4*^{tvrm267} mice and heterozygous *Adamtsl4*$^{tvrm267/+}$ or WT littermates at 1 month of age, c-waves were progressively reduced in 3- and 6-month-old homozygous *Adamtsl4*^{tvrm267} mutants. We noted that the other major components of the dc-ERG (fast oscillation (FO), LP, off-response) exhibited a comparable age-dependent reduction in amplitude.

Discussion

ADAMTS and ADAMTSL proteins are essential for regulation of ECM development and maintenance, as evidenced by the large number of Mendelian diseases that occur as a result of spontaneous mutations in humans and canines (3,33). Of the 26 members of the superfamily, 11 are unequivocally implicated in genetic diseases so far, and of those, five affect the eye. Disruptions in

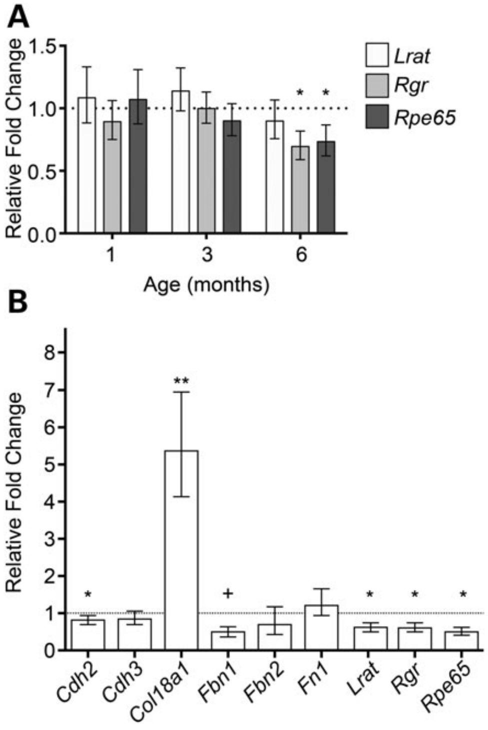

Figure 7. Expression levels of selected genes expressed in the RPE of *Adamtsl4*^{tvrm267} mutants. (**A**) Comparison by qRT–PCR of mutant and WT gene expression of *Lrat*, *Rgr* and *Rpe65* in posterior eyecups at 1, 3 and 6 months indicates progressive loss of RPE-specific expression ($n = 3$). (**B**) RPE-enriched gene expression at 6 months indicates significant reduction of *Cdh2*, trending loss of *Fbn1*, RPE-specific loss of expression of *Lrat*, *Rgr* and *Rpe65* and a significant upregulation of *Col18a1* ($n = 4$). Error bars reflect propagating error as defined in the Materials and Methods section. $^{+}P = 0.052$, $^{*}P < 0.05$, $^{**}P < 0.01$.

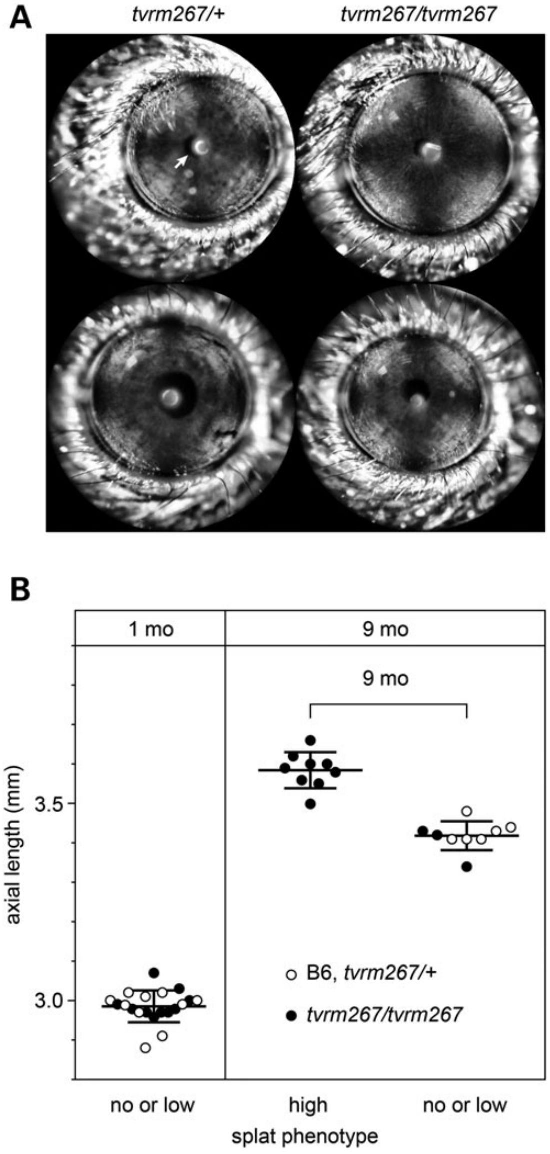

Figure 8. Assessment of pupil position and axial length of *Adamtsl4*^{tvrm267} mutants. (**A**) Normal pupil images (white arrow) from both heterozygous and homozygous *Adamtsl4*^{tvrm267} mice. (**B**) Increase in the axial length of *Adamtsl4*^{tvrm267} eyes with increasing RPE lesion severity. Ocular axial length of eyes from B6 and heterozygous (*tvrm267*/+) or homozygous (*tvrm267*/*tvrm267*) *Adamtsl4* mutant mice is plotted against a measure of the RPE disease phenotype, as graded by indirect ophthalmoscopy (no, low or high splatter phenotype). At 1 month of age, when no lesions were observed, axial lengths were similar in all eyes. At 9 months of age, axial length in homozygous *Adamtsl4*^{tvrm267} eyes graded as having a high splatter phenotype was significantly increased compared with those graded as no or low, or compared with heterozygous *Adamtsl4*^{tvrm267} and B6 eyes.

ADAMTS18 are associated with microcornea and myopic chorioretinal atrophy (34). *ADAMTS9* has been associated with a higher risk for wet age-related macular degeneration (AMD) in a large-scale genome-wide association study (35), and its haploinsufficiency leads to severe anterior segment dysgenesis in mice (Dubail, J., Apte, S.S., unpublished data). Mutations in *ADAMTS10* and *ADAMTS17* cause Weill-Marchesani syndrome 1 (MIM# 277600) and Weill-Marchesani-like syndrome (MIM# 613195), respectively, characterized by microspherophakia, which is associated with nearsightedness (myopia) that worsens over time, EL and glaucoma (reviewed in 4). In humans, mutations in *ADAMTSL4* are clearly causative for EL and EL et pupillae. Our novel mouse model demonstrates that *Adamtsl4* disruption leads to EL due to ciliary zonule detachment from the lens capsule. However, while pupil location or shape is not altered in these mutants, axial length is increased as has been observed in patients bearing *ADAMTSL4* mutations (5,11). Interestingly, the eyes from *Adamtsl4*^{tvrm267} mice also had RPE abnormalities, which has not been previously reported in humans with *ADAMTSL4* mutations.

The analysis of the distribution of *Adamtsl4* mRNA in the eye and the impact of the homozygous *Adamtsl4*^{tvrm267} mutation on the zonule, taken together with published work on the formation and composition of the zonule significantly advances our understanding of zonule stability and pathology of EL (16,17,27,36). FBN1 and FBN2, the major zonule components in mice, are secreted by the non-pigmented epithelium of the ciliary body, but there is little expression by lens epithelial cells in the equatorial region (27). Thus, the assembly of zonular fibers is thought to initiate in the ciliary body and traverse the 'space' between the ciliary body and the lens epithelium. To function properly in lens suspension and accommodation force transmission, the distal end of these fibers must be securely anchored into the lens capsule. Indeed, in humans, zonule fibers have been shown to insert into the lens capsule, an ECM (BM) produced by lens epithelial cells (18). However, the components and mechanisms of anchorage of the zonule fibers to the capsular ECM or ciliary body inner limiting membrane are unknown. Early in mouse eye development, the ciliary body and the lens epithelium are

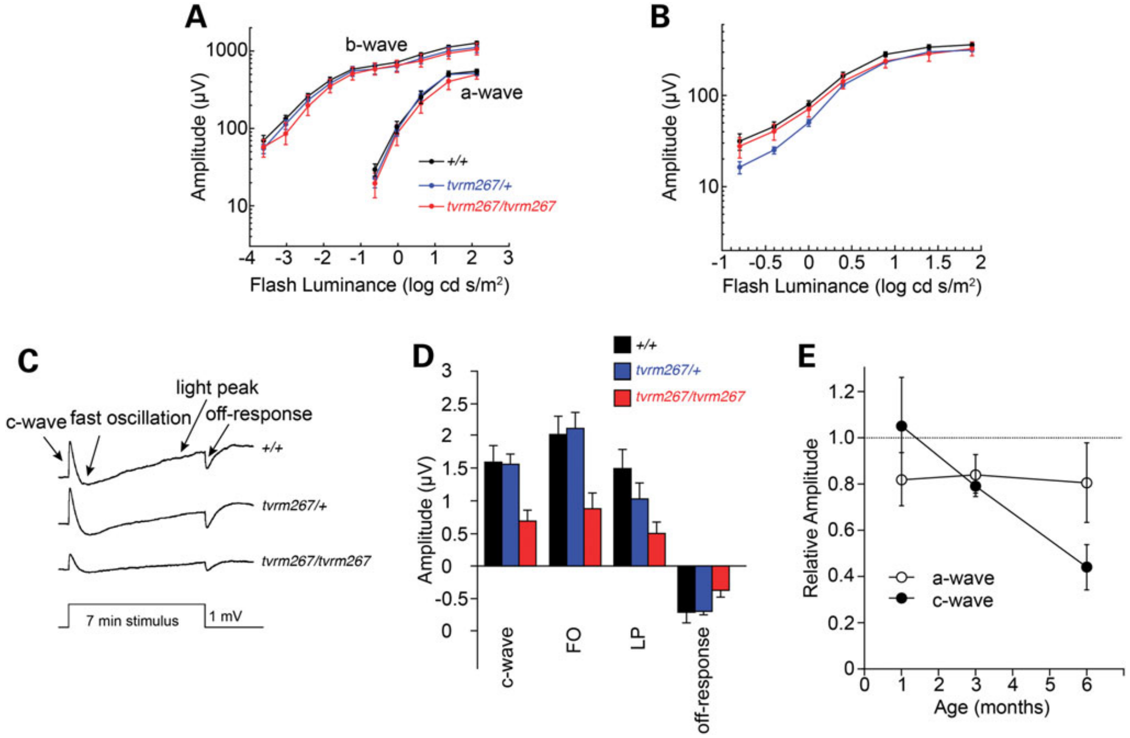

Figure 9. Electroretinographic anomalies in *Adamtsl4*^{tvrm267} mutants. (**A**) Luminance response functions for the amplitude of the major components of dark-adapted strobe flash ERGs obtained at 6 months of age. Note that a- and b-wave response functions are very similar for +/+, *tvrm267/+* and *tvrm267/tvrm267* littermates. (**B**) Luminance response functions for amplitude of the light-adapted ERGs obtained at 6 months of age. In (A and B), data points indicate the average ± SEM of 6–8 mice. (**C**) Average dc-ERGs obtained to a 7 min duration stimulus from +/+, *tvrm267/+* and *tvrm267/tvrm267* littermates. (**D**) Amplitude of the major components of the dc-ERG obtained from +/+, *tvrm267/+* and *tvrm267/tvrm267* littermates. In (C and D), waveforms and bars indicate the average of 6–11 mice and error bars in (D) indicate standard error of the mean (SEM). (**E**) Relative amplitude of the strobe flash ERG a-wave and the dc-ERG c-wave as a function of age. For each measure, average ± SEM response measures of homozygous *tvrm267* mice are expressed relative to the average response of WT and heterozygous littermates tested in parallel. Note that there is an age-related reduction in the dc-ERG c-wave while there is no age-related change in the strobe flash ERG a-wave.

in proximity to each other, which presumably facilitates formation of a nascent zonule (27).

We found that *Adamtsl4* mRNA was strongly expressed only by equatorial lens epithelium both during and beyond the embryonic and juvenile periods, and consistent with this, microfibril insertion into the lens capsule was impaired in *Adamtsl4*^{tvrm267} mutant mice. We propose that ADAMTSL4 has a specific role on the lens side of the zonule. Together with previous work showing association of ADAMTSL4 with fibrillin microfibrils, and enhancement of microfibril biogenesis in cultured cells by ADAMTSL4 (12), it is reasonable to propose that ADAMTSL4 participates in the growth or anchorage of microfibrils onto the lens capsule. ADAMTSL4 may establish the integrity of zonule anchorage early during development, such that it can withstand long-term mechanical stresses. However, the fact that *Adamtsl4* is still expressed in the lens epithelium in adult mice suggests that it may be required throughout the life span to maintain zonule attachment to the lens capsule or protect the zonule from proteolysis. Fibrillin microfibrils are susceptible to degradation by matrix metalloproteinases (MMPs), and serine proteases (37,38), which are present in the aqueous humor and the vitreous (39,40). However, if and how the zonule is turned over *in vivo* is not known.

There are few mouse models of EL. *Fbn1* mouse mutants do not develop EL because of the compensating presence of fibrillin-2 in the adult mouse zonule (17). Recently, mice lacking latent transforming growth factor beta binding protein 2 (LTBP2) were shown to develop EL, with breakage of the zonule in the bridging region, although the insertion sites in both structures appeared intact (36). The microfibrils in *Ltbp2* mutants formed normally, but appeared to be improperly bundled together, suggesting that LTBP2 had a role in forming or reinforcing lateral attachments of microfibrils in bundles, to enhance their tensile strength and/or resistance to ambient proteases (36). EL has also been described in dogs and cats, and mutations in *ADAMTS17* are known in affected terriers (33), but the underlying developmental biology has not been investigated in detail. The various ways in which specific molecular mutations affect the zonule are providing new insights into how it develops and how it is maintained during the lifespan of the organism.

The RPE defects observed in *Adamtsl4*^{tvrm267} mutants have not yet been reported in human patients with EL or EL et pupillae. However, this may be due to an ascertainment bias of the patient populations studied. For example, a murine mutation in *Mfrp* which encodes membrane frizzled-related protein and is expressed in the RPE and ciliary body (41), was first associated with a retinal degeneration phenotype (42). Later, *MFRP* was reported to be mutated in patients with extreme hyperopia (43), leading the authors to conclude that the mouse did not recapitulate the human disease due to species differences (44). However, subsequent reports showed that patients with *MFRP* mutations do indeed develop retinal degeneration (45–47). Therefore, we suspect that mutations in *ADAMTSL4* will be found in patients with retinal diseases in the human population, and this study should also prompt long-term follow-up of patients with EL for retinal problems.

Disruptions in ECM-associated proteins, including FBN2 (48), EFEMP1 (fibulin 3) (49), TIMP3 (50), collagens I and IV; elastin; fibulin 5 and 6; and MMP1, MMP2, MMP9 and MMP14 (51), have been shown to cause posterior eye disease. Evidence that ADAMTSL4 is an ECM protein (12) and is expressed in the RPE (this work, 26), together with our finding of posterior eye disease in *Adamtsl4*^{tvrm267} mice, suggests that ADAMTSL4 may be added to this list. Given the recessive inheritance of the *Adamtsl4*^{tvrm267} mutation and the reduced *Adamtsl4* transcript level, this is likely to be a loss-of-function mutation, which would lead to a reduction in the secretion of the glycoprotein into the ECM and thereby affect the homeostasis of the posterior eye. Although clear genetic and previous experimental evidence ties the function of ADAMTSL4 to fibrillin-1 in the zonule (4), it is possible that ADAMTSL4 has a function independent of fibrillin microfibrils in the RPE. In this context, our observation that the short form of *Col18a1* expression is up-regulated in RPE cells harvested from mice with a severe splatter phenotype and increased axial length, relative to controls, is of interest. While mice with *Col18a1* deficiency develop many ocular phenotypes (52), of particular interest to this study are the observed changes in the ciliary body morphogenesis (53) and the observed increase in axial length (54). Additionally, patients with disruptions in *COL18A1*, associated with Knobloch syndrome (MIM# 267750), have ocular defects such as high myopia, vitreoretinal degeneration with retinal detachment and macular abnormalities (55). COL18A1 is present in almost all BMs within the eye, and in particular, in Bruch's membrane and in the lens capsule, where it colocalizes with collagen fibrils, suggesting an anchoring role between the ECM and BM (52,56). Because we do not observe the splatter phenotype before 4 weeks of age and the elevation of *Col18a1* until 6 months, it is likely ADAMTSL4 is of primary importance in maintaining the Bruch's membrane ECM, as observed for the ciliary zonules. Alternatively, aberrant COL18A1 levels may contribute to the overall disease phenotype, especially to the increase in axial length.

In humans, there appears to be significant phenotypic variability among patients harboring *ADAMTSL4* mutations, even among affected family members within a pedigree (6,10,11), suggesting additional modification through stochastic or environmental effects or an influence of modifier genes. Similarly, variability of the disease phenotype from eye-to-eye and from mouse-to-mouse is observed in the *Adamtsl4*^{tvrm267} model; this may be due to compensatory mechanisms of local interacting factors that we currently do not fully understand. Interestingly, however, focal RPE defects similar to those in *Adamtsl4*^{tvrm267} have been reported in OXPHOS-deficient RPE (RPEΔMT) mice (29). Variability in expressivity of the disease phenotype has also been observed in patients and mice with mutations in other ECM-related genes including *TIMP3/Timp3* (50) and *EFEMP1/Efemp1* (57).

The loss of RPE basal infoldings, disorganization of the apical processes, reduced pigmentation and reduction in RPE-specific genes may be indicative of dedifferentiation of affected RPE cells. Perhaps a disruption of the ECM, which provides attachment sites for cells and relays information about the spatial position of a cell, leads to RPE cell dedifferentiation. Interestingly, gaps within the RPE cell layer were not observed, possibly owing to the importance of the maintenance of the RPE as a retinal–blood barrier. Subretinal pigmented cells observed in *Adamtsl4*^{tvrm267} mice may correspond to sloughed RPE cells, which potentially arise from mechanisms that maintain RPE integrity by extruding cells from the epithelial sheet (58). Similar histopathological changes are observed in AMD donor samples (59). However, we cannot exclude the possibility that pigmented cells may correspond to infiltrating immune cells, as have been observed in mouse models with retinal degenerative disease (42,60,61). In the time frame studied, characteristic features of sub-RPE basal laminar deposits were not observed in *Adamtsl4*^{tvrm267} homozygous mutants, although we noted accumulation of amorphous subretinal material (Fig. 5D). Therefore, further characterization of this model is necessary to determine whether it develops later stage AMD-like characteristics. That issue aside, the *Adamtsl4*^{tvrm267} mouse model may provide important clues about the mechanisms that may underlie the early changes observed in AMD eyes.

In summary, this novel ENU generated *Adamtsl4*^{tvrm267} model recapitulates the EL and increased axial length observed in affected humans and gives new insight into the pathogenic events underlying EL. What is not understood, and arises as an interesting question for future study, is how the zonule microfibrils are anchored in the lens capsule, or maintained after formation (e.g. resistance to ambient proteases). These are likely to be the defective processes in *Adamtsl4*^{tvrm267} homozygous mutants. In addition, the RPE phenotype opens new avenues of inquiry about the role of ADAMTSL4 in the homeostasis of the posterior eye, and how the loss of its function leads to the RPE cell dedifferentiation. Further characterization and investigation of this model is likely to provide important information regarding the mechanisms necessary for the maintenance of the ocular ECM. This study underscores the importance of members of the ADAMTS superfamily in the formation and/or maintenance of zonule fibers and the RPE. In addition, the *Adamtsl4*^{tvrm267} model provides a novel tool for further exploration of the molecular function of ADAMTSL4 in the eye, and may yield novel mechanistic insights into the role of ADAMTSL4 in ocular disease.

Materials and Methods

Origin of mutant mice and husbandry

Homozygous *tvrm267* mice were identified in a B6 G3 ENU mutagenesis screen (62) from the TVRM program (19) by an unusual pigmentation defect detected by indirect ophthalmoscopy. Mice, bred and housed in the Research Animal Facility, were provided a NIH 6% fat diet *ad libitum*, and acidified water in a vivarium with a 12 h light/12 h dark cycle. Procedures used in the experiments were approved by the Institutional Animal Care and Use Committee and were conducted in accordance with the ARVO Statement for the Use of Animals in Ophthalmic and Vision Research.

Linkage analysis was carried out in an F2 homozygous C57BL/6J-*tvrm267* and C3A.BLiA-*Pde6b*$^{+}$*/J* intercross to identify the chromosomal location of the mutation. Age-matched B6 mice, and *tvrm267*/+ or WT siblings were used as controls in the characterization studies of homozygous *tvrm267* mutants.

Genetic mapping and sequence analysis

Tail DNA was isolated from mice generated by the F2 intercross described above, according to Buffone and Darlington (63). DNA samples from 10 affected and 10 unaffected F2 offspring were pooled and subjected to a genome-wide scan in which 48 robust simple sequence length polymorphic (SSLP) markers known to differ between B6 and C3A.BLiA-*Pde6b*$^{+}$*/J* were used (64). For PCR amplification, 25 ng DNA was used in a 10 µl reaction volume containing 50 mm KCl, 10 mm Tris–Cl, pH 8.3, 2.5 mm $MgCl_2$, 0.2 mm oligonucleotides, 200 µM dNTP and 0.25 U *Taq* DNA polymerase. The reactions, which were initially denatured for 2 min at 95°C, were subjected to 50 cycles of 20 s at 94°C, 20 s at 50°C, 30 s at 72°C and a 3-min extension at 72°C. PCR products were separated by electrophoresis on a 4% MetaPhor (Lonza) agarose gel and visualized under UV light after staining with ethidium bromide. Once a map position was identified on Chromosome 3, samples were tested individually to confirm the linkage. The map position was refined in a high-resolution intercross involving 165 F2 mice of the intercross described.

To identify the causative mutation, a whole mouse exome library of a homozygous *Adamtsl4*^{tvrm267} mutant was constructed, using fragmented genomic DNA (1 µg) to a peak size of 300 bp by sonicating for 30 s power on, 30 s power off on low power for a total of 10 min using a Bioruptor UCD-200TM-EX (Diagenode). The pre-capture paired end library was constructed using the Illumina TruSeq DNA Sample Preparation Kit (Illumina, part number FC-121-100) with no size selection step and 18 cycles of PCR. The pre-capture library was hybridized to the Mouse Exome (Roche NimbleGen, Reference # 9999042611) capture probe set according to the manufacturer's instructions. The sequencing library was quantified by qPCR, pooled with two similar libraries and sequenced on a single lane of a HiSeq 2000 sequencer (Illumina) using a 2 × 100 bases (paired end) sequencing protocol.

High-throughput sequence data were sorted using a local JAX Galaxy interface pipeline (65–67). Sequence reads were quality assessed using FastQC v0.5 (http://www.bioinformatics.babraham.ac.uk/projects/fastqc/) and aligned to the mouse reference genome (mm10) from UCSC, released December 2011, using BWA v1.2.3 (68). PCR duplicates were removed using SAMtools rmdup v.1.0.0 (69). SNPs and indels were called using SAMtools mpileup v1.0.0 (69) and genomic and functional annotations were assigned to the variants using SnpEff v0.9 (70).

To confirm the identified mutation, we designed primer pairs (Adamtsl4seqF, CTTCCCTCCTCAGATGATCTTTC and Adamtsl4-seqR, CCCACTTGTTTCCAGTATCCA) to amplify and sequence the *Adamtsl4* genomic region containing the mutation in both the segregating mapping and the maintenance colonies. An aliquot of the PCR reaction product was electrophoresed on a 1% agarose gel to confirm single fragment amplification. PCR product was purified using AMPure XP magnetic beads (Agencourt), sequenced using BigDye Terminator Cycle Sequencing Chemistry and separated by capillary electrophoresis on Applied Biosystems 3730xl DNA Analyzer using 5 pmol/µl Adamtls4seqF sequencing primer. Concordance of the mutation with the retinal depigmentation phenotype was assessed.

RNA isolation and quantitative real-time PCR

Total RNA was isolated from posterior eyecups with the retina removed using an RNeasy Mini kit (QIAGEN). Samples were homogenized in TRIzol reagent (Life Technologies) and phase separated in 1/5 volume of chloroform. The aqueous phase was mixed with 0.5× absolute ethanol and transferred to an RNeasy Mini spin column. An on-column DNase I treatment was performed following manufacturer's recommendations. Purified total RNA was eluted in RNase-free water and quantified using a Nanodrop-1000 spectrophotometer (Thermo-Scientific). RNA was reverse-transcribed into cDNA with RETROscript Reverse Transcription kit according to manufacturer's recommendations using random priming (Life Technologies).

Enrichment of RPE-specific total RNA was carried out as described (71). Briefly, the RPE from a single posterior eyecup with the retina removed was solubilized in RNAprotect Cell Reagent (QIAGEN) for 10 min at room temperature (RT) with periodic agitation. The eyecup was removed and the remaining solubilized cell suspension was pelleted and supernatant discarded. Individual pellets were pooled per sample and processed for RNA isolation using the RNeasy Micro Kit (QIAGEN). An on-column DNase I treatment was performed following manufacturer's recommendations. Purified total RNA was eluted in RNase-free water and quantified using a Nanodrop-1000 spectrophotometer (Thermo-Scientific). RNA was reverse-transcribed into cDNA with RETROscript Reverse Transcription kit according to manufacturer's instructions using random priming (Life Technologies).

Lens were dissected from enucleated eyes from 6-month-old mice and placed in RNAprotect Cell Reagent (QIAGEN). Pooled samples were homogenized and pelleted. Supernatants were removed and pellets were processed for RNA isolation as above using the RNeasy Micro Kit (QIAGEN).

qRT–PCR was performed with the iTaq Universal SYBR Green SuperMix (Bio-Rad) and gene-specific primers (Supplementary material, Table S1) using the CFX96 Real-Time PCR Detection System (Bio-Rad). The comparative CT method ($\Delta\Delta C_T$) was applied to calculate a relative fold change in gene transcripts and was quantified using $2^{-\Delta\Delta CT}$ with *Actb* as an internal calibrator. Melting curve analyses were performed to validate accurate amplification of the target genes. Error bars represent the additive propagation of error as calculated in Nordgard *et al.* (72).

Histological and immunohistochemical analysis

The protocols for histological and immunohistochemical assays were previously described (73). Briefly, after carbon dioxide asphyxiation, eyes were enucleated and placed in cold acetic acid/methanol solution or freshly prepared 4% paraformaldehyde (PFA) in phosphate-buffered saline (PBS) overnight at 4°C, as appropriate for the application. To visualize oxytalan fibers, eyes were embedded in paraffin and 6 µm sections were stained with specific histochemical stain for oxytalan fibers (13,14,74) and examined by light microscopy. Briefly, sections were deparaffinized and incubated for 30 min in 10% (w/v) Oxone (Sigma) dissolved in water at RT. This oxidation step allows the preferred staining of oxytalan fibers (fibrillin microfibrils) and suppresses the staining of elastic fibers, which in any case, are absent in the zonule. Sections were then rinsed with water followed by 70% ethanol and stained with Aldehyde-Fuchsin (pH 1) (Electron Microscopy Sciences) for 1 h at RT. After a washing step (95%, v/v ethanol), sections were counterstained with 1% eosin (Electron Microscopy Sciences) and after additional washing steps in 100% ethanol, slides were mounted with Cytoseal-60 (Fisher Thermo-Scientific). For immunofluorescence staining, deparaffinized sections were incubated with anti-fibrillin 1 (75), anti-fibrillin-2 (76), anti microfibril-associated glycoprotein 1 (MAGP1) (77), anti-ezrin (Sigma) and ZO-1 (Life Technologies). Antibody binding was revealed using Cy3- or Alexa Fluor 488-conjugated secondary antibodies (Jackson Immuno Research, Life Technologies) and visualized by fluorescence microscopy. For negative controls, the primary antibody was omitted. The specificity of the fibrillin-1, fibrillin-2 and MAGP1 antibodies was previously described (17). To produce an ezrin-stained/brightfield image overlay, green fluorescent images were merged with brightfield images in red channel (QImaging software). Red channel LUT was inverted to highlight the RPE and choroidal pigments in dark red.

For flatmount analysis, radially-cut posterior cups were prepared from mouse eyes fixed in ice-cold 4% (w/v) PFA in 0.75X PBS for ~1 h as described (78), except that the RPE/choroid/sclera complex was retained and stained with rhodamine-conjugated phalloidin and DAPI as described (79). Flatmounts were imaged with a 10× objective on an Axio Observer.Z1 widefield fluorescence microscope (Zeiss) equipped with a translational stage to allow tiling of the entire sample. As the flatmount samples were uneven, a z-stack (2.0 µm step size) with sufficient thickness to ensure focus in all areas of the sample was acquired at each tile. Post-acquisition processing in Fiji (80) included the use of the Extended Depth of Field plugin (81) to merge the z-stacks and the Stitching plugin (82) to generate a blended mosaic of the merged tiles. An identical approach was used to obtain higher resolution tiled images of the same samples, except that a 40× objective was used with a step size of 0.28 µm. Image brightness and contrast were adjusted in Fiji.

Morphometric analysis of processed flatmount images was performed in Fiji. To assess RPE structural changes, cells were segmented manually with the Cell Magic Wand tool from projected 40× image datasets based on the phalloidin-stained circumferential F-actin. Measurements in Fiji included total area and Feret diameter. For analysis of lesion distribution, lesions were segmented manually from 10× mosaics with the Cell Magic Wand tool based on decreased phalloidin staining. Lesions near radial cuts were excluded from analysis because of possible artifacts introduced by the cuts. Large darkened patches occasionally observed in the periphery were also excluded, as these regions did not show evidence of altered RPE cell morphology and were likely due to artifactual transfer of a patch of apical RPE to the retina during flatmount preparation. Fractional lesion area was determined by fusing contours to create a single contour for each lesion, measuring the area of each, and dividing the sum of lesion areas in the inferior RPE by the total lesion area. Fractional lesion area in the inferior RPE was graphed and analyzed by a one-sample, two-sided *t*-test in Prism (GraphPad). A *P* value of <0.05 was considered significant.

RNA *in situ* hybridization

Mouse tissue was fixed in 4% PFA overnight at 4°C, processed and paraffin embedded. Fresh 6 µm sections were used for ISH using RNAscope (all materials from Advanced Cell Diagnostics) following the manufacturer's protocol. All steps requiring incubation at 40°C were performed in the HybEZ Oven. Binding of the specific probe against mouse *Adamtsl4* mRNA (#316441) was detected with the RNAscope 2.0 HD detection kit 'RED'. Probes against mouse peptidylprolyl isomerase B (Cyclophilin B, *Ppib*) or bacterial dihydrodipicolinate reductase (*dapB*) mRNA (#313911, #310043) were used as positive and negative controls, respectively. Images were collected using a Leica DM5500B upright microscope and post-acquisition image processing was performed using Corel PHOTO-PAINT. To enhance the red signal in highly pigmented tissues such as the RPE or the iris, the 'brightness/contrast/intensity' settings and the 'hue/saturation' settings were modulated in order to enhance the red color of the ISH signal and reduce the dark and blue colors of the pigment and the hematoxylin counterstain.

Electron microscopy

For transmission electron microscopy, mice underwent intracardiac perfusion with PBS followed by fixative (phosphate buffered 2.5% glutaraldehyde/2% PFA solution in Sorensen buffer). Eyes were enucleated and incubated in ice-cold fixative for 30 min. The cornea and lens were removed and eyecups were fixed for an additional 4 h followed by overnight fixation in 1/10 concentration of fixative. The following morning, eye cups were cut into small triangles, and post-fixed with 1% osmium tetroxide for 2 h. The tissues were rinsed through a series of alcohol gradients and dehydrated blocks were embedded in epoxy resin. Tissue sections were cut and stained by uranyl acetate and lead citrate and examined under a transmission JEM-1230 electron microscope (JEOL).

For scanning electron microscopy, eyes were cut along the posterior end of the limbus such that the ciliary body remained attached to the lens. The anterior segment was fixed in 3% glutaraldehyde/1% PFA solution in cacodylate buffer for 4 h at 4°C and rinsed overnight in buffer. Tissues were post-fixed in osmium tetroxide, dehydrated, dried with hexamethyldisilazane, mounted and sputter coated. Specimens were examined by an S-3000N scanning electron microscope (Hitachi Technologies America).

Electroretinography

ERGs were obtained using two stimuli and recording protocols (32). In both cases, mice were dark-adapted overnight and anesthetized with ketamine (80 mg/kg) and xylazine (16 mg/kg). The corneas were anesthetized (1% proparacaine HCl), and the pupils were dilated (1% mydriacyl, 2.5% phenylephrine HCl, 1% cyclopentolate). Mice were placed on a temperature-regulated heating pad throughout each recording session. Homozygous *Adamtsl4*^{tvrm267} mice and age-matched littermates (heterozygous *tvrm267* or WT) were tested at 1, 3 and 6 months of age.

To measure ERG components generated by the outer neural retina, responses were recorded from the corneal surface using a stainless steel electrode that was wetted with 0.7% methylcellulose. Needle electrodes placed in the cheek and the tail served as reference and ground leads, respectively. Responses were differentially amplified (0.3–1500 Hz), averaged and stored using a UTAS E-3000 signal averaging system (LKC Technologies). Responses were first obtained to stimuli presented in the dark. Flash stimuli were presented in an LKC ganzfeld and ranged in luminance from −3.6 to 2.1 log cd s/m^2; interstimulus intervals increased from 4 s at the lowest flash luminance to 61 s at the highest stimulus levels. Stimuli were presented in order of increasing luminance and at least two successive responses were averaged for each stimulus condition. A steady rod-desensitizing adapting field was then presented within the ganzfeld bowl. After allowing a 7 min period of light adaptation, cone ERGs were recorded to flashes superimposed upon the adapting field. Flash luminance ranged from −0.8 to 1.9 log cd s/m^2 and responses to 50 flashes presented at 2.1 Hz were averaged at each intensity level.

The amplitude of the a-wave was measured 8 ms after flash onset from the pre-stimulus baseline. The amplitude of the b-wave was measured from the a-wave trough to the peak of the b-wave or, if no a-wave was present, from the pre-stimulus baseline. Implicit times were measured from the time of flash onset to the a-wave trough or the b-wave peak.

Components of the dc-ERG generated by the RPE were recorded with an Ag/AgCl electrode bridged to the corneal surface with Hanks' balanced salt solution in response to stimuli presented for 7 min. The amplitude of the c-wave was measured from the pre-stimulus baseline to the peak of the c-wave. The amplitude of the FO was measured from the c-wave peak to the trough of the FO. The amplitude of the light peak (LP) was measured from the FO trough to the asymptotic value. The amplitude of the off-response was measured from the LP asymptote to the peak of the off-response.

Indirect ophthalmoscopy and fundus photography

Pupils were dilated with 1% atropine, and mice were dark adapted before viewing retinas with an indirect ophthalmoscope and a

60-D aspheric lens. Bright field fundus imaging was used to document fundus changes and to detect subtle changes that cannot be observed by indirect ophthalmoscopy. Images were acquired with a Micron III or Micron IV retinal camera (Phoenix Research Laboratories) and processed as described (79). To correct for illumination inhomogeneity and vignetting, fundus images were processed further in Fiji with the Polynomial Shading Corrector (10th degree polynomial in *x* and *y*, 10% regularization of peak). Brightness and contrast were adjusted in Fiji (80).

Axial length

The axial length of eyes from mutant and control mice was assessed using Vernier calipers as described (83). Eyes were enucleated and briefly stored in PBS to minimize dehydration. Both eyes were measured three times within 5–10 min of enucleation. Repeated measures of the same eye had a relative standard deviation of 1.5 ± 0.9% and the mean difference in axial length between eyes of the same mouse was 0.7 ± 2.0%, indicating the reproducibility of the method.

Supplementary Material

Supplementary Material is available at *HMG* online.

Acknowledgements

We thank JAX Multimedia Services for graphical assistance, JAX Genome Sciences for sequencing and Lesley Bechtold and Pete Finger for EM imaging services. We thank Dr Dieter Reinhardt (McGill University Montreal, Canada) and Dr Robert Mecham (Washington University, St. Louis, USA) for kindly providing fibrillin-1, -2 and MAGP1 antibodies.

Conflict of Interest statement. None declared.

Funding

This work was supported by the National Institutes of Health (EY016501 to P.M.N. and EY021151 to S.A.); a Challenge Grant from Research to Prevent Blindness to Cleveland Clinic Lerner College of Medicine of Case Western Reserve University; the Foundation Fighting Blindness (N.S.P.); Department of Veteran's Affairs (Research Career Scientist Award to N.S.P.); and the Marfan Foundation (to D.H.). Core services at The Jackson Laboratory were supported by an institutional grant (CA34196).

References

1. Mouw, J.K., Ou, G. and Weaver, V.M. (2014) Extracellular matrix assembly: a multiscale deconstruction. *Nat. Rev. Mol. Cell Biol.*, **15**, 771–785.
2. Booij, J.C., Baas, D.C., Beisekeeva, J., Gorgels, T.G. and Bergen, A.A. (2010) The dynamic nature of Bruch's membrane. *Prog. Retin. Eye Res.*, **29**, 1–18.
3. Dubail, J. and Apte, S.S. (2015) Insights on ADAMTS proteases and ADAMTS-like proteins from mammalian genetics. *Matrix Biol.*, **44–46**, 24–37.
4. Hubmacher, D. and Apte, S.S. (2015) ADAMTS proteins as modulators of microfibril formation and function. *Matrix Biol.*, doi: 10.1016/j.matbio.2015.05.004.
5. Chandra, A., Aragon-Martin, J.A., Hughes, K., Gati, S., Reddy, M.A., Deshpande, C., Cormack, G., Child, A.H., Charteris, D. G. and Arno, G. (2012) A genotype–phenotype comparison of *ADAMTSL4* and *FBN1* in isolated ectopia lentis. *Invest. Ophthalmol. Vis. Sci.*, **53**, 4889–4896.
6. Ahram, D., Sato, T.S., Kohilan, A., Tayeh, M., Chen, S., Leal, S., Al-Salem, M. and El-Shanti, H. (2009) A homozygous mutation in *ADAMTSL4* causes autosomal-recessive isolated ectopia lentis. *Am. J. Hum. Genet.*, **84**, 274–278.
7. Sharifi, Y., Tjon-Fo-Sang, M.J., Cruysberg, J.R. and Maat-Kievit, A.J. (2013) Ectopia lentis et pupillae in four generations caused by novel mutations in the *ADAMTSL4* gene. *Br. J. Ophthalmol.*, **97**, 583–587.
8. Chandra, A., Aragon-Martin, J.A., Sharif, S., Parulekar, M., Child, A. and Arno, G. (2013) Craniosynostosis with ectopia lentis and a homozygous 20-base deletion in *ADAMTSL4*. *Ophthalmic Genet.*, **34**, 78–82.
9. Christensen, A.E., Fiskerstrand, T., Knappskog, P.M., Boman, H. and Rodahl, E. (2010) A novel *ADAMTSL4* mutation in autosomal recessive ectopia lentis et pupillae. *Invest. Ophthalmol. Vis. Sci.*, **51**, 6369–6373.
10. Rødahl, E., Christensen, A.E., Fiskerstrand, T., Knappskog, P. M. and Boman, H. (1993–2015) ADAMTSL4-related eye disorders. In Pagon, R.A. *et al.* (eds), In *GeneReviews*®, University of Washington, Seattle, Seattle, WA.
11. Neuhann, T.M., Stegerer, A., Riess, A., Blair, E., Martin, T., Wieser, S., Klas, R., Bouman, A., Kuechler, A. and Rittinger, O. (2015) ADAMTSL4-associated isolated ectopia lentis: further patients, novel mutations and a detailed phenotype description. *Am. J. Med. Genet.*, **167**, 2376–2381.
12. Gabriel, L.A., Wang, L.W., Bader, H., Ho, J.C., Majors, A.K., Hollyfield, J.G., Traboulsi, E.I. and Apte, S.S. (2012) ADAMTSL4, a secreted glycoprotein widely distributed in the eye, binds fibrillin-1 microfibrils and accelerates microfibril biogenesis. *Invest. Ophthalmol. Vis. Sci.*, **53**, 461–469.
13. Fullmer, H.M. and Lillie, R.D. (1958) The oxytalan fiber: a previously undescribed connective tissue fiber. *J. Histochem. Cytochem.*, **6**, 425–430.
14. Garner, A. and Alexander, R.A. (1986) Histochemistry of elastic and related fibres in the human eye in health and disease. *Histochem. J.*, **18**, 405–412.
15. Wheatley, H.M., Traboulsi, E.I., Flowers, B.E., Maumenee, I.H., Azar, D., Pyeritz, R.E. and Whittum-Hudson, J.A. (1995) Immunohistochemical localization of fibrillin in human ocular tissues. Relevance to the Marfan syndrome. *Arch. Ophthalmol.*, **113**, 103–109.
16. Hubmacher, D., Reinhardt, D.P., Plesec, T., Schenke-Layland, K. and Apte, S.S. (2014) Human eye development is characterized by coordinated expression of fibrillin isoforms. *Invest. Ophthalmol. Vis. Sci.*, **55**, 7934–7944.
17. Beene, L.C., Wang, L.W., Hubmacher, D., Keene, D.R., Reinhardt, D.P., Annis, D.S., Mosher, D.F., Mecham, R.P., Traboulsi, E.I. and Apte, S.S. (2013) Nonselective assembly of fibrillin 1 and fibrillin 2 in the rodent ocular zonule and in cultured cells: implications for Marfan syndrome. *Invest. Ophthalmol. Vis. Sci.*, **54**, 8337–8344.
18. Mir, S., Wheatley, H.M., Hussels, I.E., Whittum-Hudson, J.A. and Traboulsi, E.I. (1998) A comparative histologic study of the fibrillin microfibrillar system in the lens capsule of normal subjects and subjects with Marfan syndrome. *Invest. Ophthalmol. Vis. Sci.*, **39**, 84–93.
19. Won, J., Shi, L.Y., Hicks, W., Wang, J., Naggert, J.K. and Nishina, P.M. (2012) Translational vision research models program. *Adv. Exp. Med. Biol.*, **723**, 391–397.
20. Dietrich, W., Katz, H., Lincoln, S.E.,, Shin, H.S., Friedman, J., Dracopoli, N.C. and Lander, E.S. (1992) A genetic map of the mouse suitable for typing intraspecific crosses. *Genetics*, **131**, 423–447.

21. Zhou, X.M., Wang, Y., Zhao, L., Yu, W.H., Fan, N., Yan, N.H., Su, Q., Liang, Y.Q., Wang, Y., Li, L.P. *et al.* (2015) Novel compound heterozygous mutations identified in *ADAMTSL4* gene in a Chinese family with isolated ectopia lentis. *Acta Ophthalmol.*, **93**, e91–e92.
22. Greene, V.B., Stoetzel, C., Pelletier, V., Perdomo-Trujillo, Y., Liebermann, L., Marion, V., De Korvin, H., Boileau, C., Dufier, J.L. and Dollfus, H. (2010) Confirmation of *ADAMTSL4* mutations for autosomal recessive isolated bilateral ectopia lentis. *Ophthalmic Genet.*, **31**, 47–51.
23. Aragon-Martin, J.A., Ahnood, D., Charteris, D.G., Saggar, A., Nischal, K.K., Comeglio, P., Chandra, A., Child, A.H. and Arno, G. (2010) Role of *ADAMTSL4* mutations in *FBN1* mutation-negative ectopia lentis patients. *Hum. Mutat.*, **31**, E1622–E1631.
24. Neuhann, T.M., Artelt, J., Neuhann, T.F., Tinschert, S. and Rump, A. (2011) A homozygous microdeletion within *ADAMTSL4* in patients with isolated ectopia lentis: evidence of a founder mutation. *Invest. Ophthalmol. Vis. Sci.*, **52**, 695–700.
25. Kuzmiak, H.A. and Maquat, L.E. (2006) Applying nonsense-mediated mRNA decay research to the clinic: progress and challenges. *Trends Mol. Med.*, **12**, 306–316.
26. Chandra, A., Jones, M., Cottrill, P., Eastlake, K., Limb, G.A. and Charteris, D.G. (2013) Gene expression and protein distribution of ADAMTSL-4 in human iris, choroid and retina. *Br. J. Ophthalmol.*, **97**, 1208–1212.
27. Shi, Y., Tu, Y., De Maria, A., Mecham, R.P. and Bassnett, S. (2013) Development, composition, and structural arrangements of the ciliary zonule of the mouse. *Invest. Ophthalmol. Vis. Sci.*, **54**, 2504–2515.
28. Mehalow, A.K., Kameya, S., Smith, R.S., Hawes, N.L., Denegre, J.M., Young, J.A., Bechtold, L., Haider, N.B., Tepass, U., Heckenlively, J.R. *et al.* (2003) *CRB1* is essential for external limiting membrane integrity and photoreceptor morphogenesis in the mammalian retina. *Hum. Mol. Genet.*, **12**, 2179–2189.
29. Zhao, C., Yasumura, D., Li, X., Matthes, M., Lloyd, M., Nielsen, G., Ahern, K., Snyder, M., Bok, D., Dunaief, J.L. *et al.* (2011) mTOR-mediated dedifferentiation of the retinal pigment epithelium initiates photoreceptor degeneration in mice. *J. Clin. Invest.*, **121**, 369–383.
30. Bonilha, V.L., Finnemann, S.C. and Rodriguez-Boulan, E. (1999) Ezrin promotes morphogenesis of apical microvilli and basal infoldings in retinal pigment epithelium. *J. Cell. Biol.*, **147**, 1533–1548.
31. Soundararajan, R., Won, J., Stearns, T.M., Charette, J.R., Hicks, W.L., Collin, G.B., Naggert, J.K., Krebs, M.P. and Nishina, P.M. (2014) Gene profiling of postnatal *Mfrp*^{rd6} mutant eyes reveals differential accumulation of *Prss56*, visual cycle and phototransduction mRNAs. *PLoS One*, **9**, e110299.
32. Patil, H., Saha, A., Senda, E., Cho, K.I., Haque, M., Yu, M., Qiu, S., Yoon, D., Hao, Y., Peachey, N.S. *et al.* (2014) Selective impairment of a subset of Ran-GTP-binding domains of ran-binding protein 2 (Ranbp2) suffices to recapitulate the degeneration of the retinal pigment epithelium (RPE) triggered by *Ranbp2* ablation. *J. Biol. Chem.*, **289**, 29767–29789.
33. Gould, D., Pettitt, L., McLaughlin, B., Holmes, N., Forman, O., Thomas, A., Ahonen, S., Lohi, H., O'Leary, C., Sargan, D. *et al.* (2011) *ADAMTS17* mutation associated with primary lens luxation is widespread among breeds. *Vet. Ophthalmol.*, **14**, 378–384.
34. Aldahmesh, M.A., Alshammari, M.J., Khan, A.O., Mohamed, J.Y., Alhabib, F.A. and Alkuraya, F.S. (2013) The syndrome of microcornea, myopic chorioretinal atrophy, and telecanthus (MMCAT) is caused by mutations in *ADAMTS18*. *Hum. Mutat.*, **34**, 1195–1199.
35. Helisalmi, S., Immonen, I., Losonczy, G., Resch, M.D., Benedek, S., Balogh, I., Papp, A., Berta, A., Uusitupa, M., Hiltunen, M. *et al.* (2014) *ADAMTS9* locus associates with increased risk of wet AMD. *Acta Ophthalmol. (Copenh.)*, **92**, e410.
36. Inoue, T., Ohbayashi, T., Fujikawa, Y., Yoshida, H., Akama, T. O., Noda, K., Horiguchi, M., Kameyama, K., Hata, Y., Takahashi, K. *et al.* (2014) Latent TGF-beta binding protein-2 is essential for the development of ciliary zonule microfibrils. *Hum. Mol. Genet.*, **23**, 5672–5682.
37. Hindson, V.J., Ashworth, J.L., Rock, M.J., Cunliffe, S., Shuttleworth, C.A. and Kielty, C.M. (1999) Fibrillin degradation by matrix metalloproteinases: identification of amino- and carboxy-terminal cleavage sites. *FEBS Lett.*, **452**, 195–198.
38. Kielty, C.M., Woolley, D.E., Whittaker, S.P. and Shuttleworth, C.A. (1994) Catabolism of intact fibrillin microfibrils by neutrophil elastase, chymotrypsin and trypsin. *FEBS Lett.*, **351**, 85–89.
39. Jia, Y., Hu, D.N., Zhu, D., Zhang, L., Gu, P., Fan, X. and Zhou, J. (2014) MMP-2, MMP-3, TIMP-1, TIMP-2, and TIMP-3 protein levels in human aqueous humor: relationship with axial length. *Invest. Ophthalmol. Vis. Sci.*, **55**, 3922–3928.
40. Weinstein, W.L., Dietrich, U.M., Sapienza, J.S., Carmichael, K.P., Moore, P.A. and Krunkosky, T.M. (2007) Identification of ocular matrix metalloproteinases present within the aqueous humor and iridocorneal drainage angle tissue of normal and glaucomatous canine eyes. *Vet. Ophthalmol.*, **10**(Suppl. 1), 108–116.
41. Kameya, S., Hawes, N.L., Chang, B., Heckenlively, J.R., Naggert, J.K. and Nishina, P.M. (2002) *Mfrp*, a gene encoding a frizzled related protein, is mutated in the mouse retinal degeneration 6. *Hum. Mol. Genet.*, **11**, 1879–1886.
42. Hawes, N.L., Chang, B., Hageman, G.S., Nusinowitz, S., Nishina, P.M., Schneider, B.S., Smith, R.S., Roderick, T.H., Davisson, M.T. and Heckenlively, J.R. (2000) Retinal degeneration 6 (*rd6*): a new mouse model for human retinitis punctata albescens. *Invest. Ophthalmol. Vis. Sci.*, **41**, 3149–3157.
43. Sundin, O.H., Leppert, G.S., Silva, E.D., Yang, J.-M., Dharmaraj, S., Maumenee, I.H., Santos, L.C., Parsa, C.F., Traboulsi, E.I., Broman, K.W. *et al.* (2005) Extreme hyperopia is the result of null mutations in *MFRP*, which encodes a Frizzled-related protein. *Proc. Natl Acad. Sci. U. S. A.*, **102**, 9553–9558.
44. Sundin, O.H. (2005) The mouse's eye and *Mfrp*: not quite human. *Ophthalmic Genet.*, **26**, 153–155.
45. Beryozkin, A., Zelinger, L., Bandah-Rozenfeld, D., Shevach, E., Harel, A., Storm, T., Sagi, M., Eli, D., Merin, S., Banin, E. *et al.* (2014) Identification of mutations causing inherited retinal degenerations in the Israeli and Palestinian populations using homozygosity mapping. *Invest. Ophthalmol. Vis. Sci.*, **55**, 1149–1160.
46. Kannabiran, C., Singh, H., Sahini, N., Jalali, S. and Mohan, G. (2012) Mutations in *TULP1*, *NR2E3*, and *MFRP* genes in Indian families with autosomal recessive retinitis pigmentosa. *Mol. Vis.*, **18**, 1165–1174.
47. Dinculescu, A., Estreicher, J., Zenteno, J.C., Aleman, T.S., Schwartz, S.B., Huang, W.C., Roman, A.J., Sumaroka, A., Li, Q., Deng, W.T. *et al.* (2012) Gene therapy for retinitis pigmentosa caused by *MFRP* mutations: human phenotype and preliminary proof of concept. *Hum. Gene Ther.*, **23**, 367–376.
48. Ratnapriya, R., Zhan, X., Fariss, R.N., Branham, K.E., Zipprer, D., Chakarova, C.F., Sergeev, Y.V., Campos, M.M., Othman, M., Friedman, J.S. *et al.* (2014) Rare and common variants in

extracellular matrix gene Fibrillin 2 (*FBN2*) are associated with macular degeneration. *Hum. Mol. Genet.*, **23**, 5827–5837.

49. Marmorstein, L. (2004) Association of *EFEMP1* with malattia leventinese and age-related macular degeneration: a minireview. *Ophthalmic Genet.*, **25**, 219–226.
50. Stohr, H. and Anand-Apte, B. (2012) A review and update on the molecular basis of pathogenesis of Sorsby fundus dystrophy. *Adv. Exp. Med. Biol.*, **723**, 261–267.
51. Nita, M., Strzalka-Mrozik, B., Grzybowski, A., Mazurek, U. and Romaniuk, W. (2014) Age-related macular degeneration and changes in the extracellular matrix. *Med. Sci. Monit.*, **20**, 1003–1016.
52. Fukai, N., Eklund, L., Marneros, A.G., Oh, S.P., Keene, D.R., Tamarkin, L., Niemela, M., Ilves, M., Li, E., Pihlajaniemi, T. *et al.* (2002) Lack of collagen XVIII/endostatin results in eye abnormalities. *EMBO J.*, **21**, 1535–1544.
53. Ylikarppa, R., Eklund, L., Sormunen, R., Kontiola, A.I., Utriainen, A., Maatta, M., Fukai, N., Olsen, B.R. and Pihlajaniemi, T. (2003) Lack of type XVIII collagen results in anterior ocular defects. *FASEB J.*, **17**, 2257–2259.
54. Aikio, M., Hurskainen, M., Brideau, G., Hagg, P., Sormunen, R., Heljasvaara, R., Gould, D.B. and Pihlajaniemi, T. (2013) Collagen XVIII short isoform is critical for retinal vascularization, and overexpression of the Tsp-1 domain affects eye growth and cataract formation. *Invest. Ophthalmol. Vis. Sci.*, **54**, 7450–7462.
55. Seppinen, L. and Pihlajaniemi, T. (2011) The multiple functions of collagen XVIII in development and disease. *Matrix Biol.*, **30**, 83–92.
56. Uechi, G., Sun, Z., Schreiber, E.M., Halfter, W. and Balasubramani, M. (2014) Proteomic view of basement membranes from human retinal blood vessels, inner limiting membranes, and lens capsules. *J. Proteome Res.*, **13**, 3693–3705.
57. Marmorstein, L.Y., McLaughlin, P.J., Peachey, N.S., Sasaki, T. and Marmorstein, A.D. (2007) Formation and progression of sub-retinal pigment epithelium deposits in *Efemp1* mutation knock-in mice: a model for the early pathogenic course of macular degeneration. *Hum. Mol. Genet.*, **16**, 2423–2432.
58. Macara, I.G., Guyer, R., Richardson, G., Huo, Y. and Ahmed, S. M. (2014) Epithelial homeostasis. *Curr. Biol.*, **24**, R815–R825.
59. Zanzottera, E.C., Messinger, J.D., Ach, T., Smith, R.T., Freund, K.B. and Curcio, C.A. (2015) The project MACULA retinal pigment epithelium grading system for histology and optical coherence tomography in age-related macular degeneration. *Invest. Ophthalmol. Vis. Sci.*, **56**, 3253–3268.
60. Fogerty, J. and Besharse, J.C. (2011) 174delG mutation in mouse *MFRP* causes photoreceptor degeneration and RPE atrophy. *Invest. Ophthalmol. Vis. Sci.*, **52**, 7256–7266.
61. Jadeja, S., Barnard, A.R., McKie, L., Cross, S.H., White, J.K., Robertson, M., Budd, P.S., MacLaren, R.E. and Jackson, I.J. (2015) Mouse *Slc9a8* mutants exhibit retinal defects due to retinal pigmented epithelium dysfunction. *Invest. Ophthalmol. Vis. Sci.*, **56**, 3015–3026.
62. Concepcion, D., Seburn, K.L., Wen, G., Frankel, W.N. and Hamilton, B.A. (2004) Mutation rate and predicted phenotypic target sizes in ethylnitrosourea-treated mice. *Genetics*, **168**, 953–959.
63. Buffone, G.J. and Darlington, G.J. (1985) Isolation of DNA from biological specimens without extraction with phenol. *Clin. Chem.*, **31**, 164–165.
64. Taylor, B.A., Navin, A. and Phillips, S.J. (1994) PCR-amplification of simple sequence repeat variants from pooled DNA samples for rapidly mapping new mutations of the mouse. *Genomics*, **21**, 626–632.
65. Blankenberg, D., Von Kuster, G., Coraor, N., Ananda, G., Lazarus, R., Mangan, M., Nekrutenko, A. and Taylor, J. (2010) Galaxy: a web-based genome analysis tool for experimentalists. *Curr. Protoc. Mol. Biol.*, Chapter 19, Unit 1910.1–21.
66. Giardine, B., Riemer, C., Hardison, R.C., Burhans, R., Elnitski, L., Shah, P., Zhang, Y., Blankenberg, D., Albert, I., Taylor, J. *et al.* (2005) Galaxy: a platform for interactive large-scale genome analysis. *Genome Res.*, **15**, 1451–1455.
67. Goecks, J., Nekrutenko, A. and Taylor, J. (2010) Galaxy: a comprehensive approach for supporting accessible, reproducible, and transparent computational research in the life sciences. *Genome Biol.*, **11**, R86.
68. Li, H. and Durbin, R. (2009) Fast and accurate short read alignment with Burrows-Wheeler transform. *Bioinformatics*, **25**, 1754–1760.
69. Li, H., Handsaker, B., Wysoker, A., Fennell, T., Ruan, J., Homer, N., Marth, G., Abecasis, G. and Durbin, R. (2009) The Sequence Alignment/Map format and SAMtools. *Bioinformatics*, **25**, 2078–2079.
70. Cingolani, P., Platts, A., Wang le, L., Coon, M., Nguyen, T., Wang, L., Land, S.J., Lu, X. and Ruden, D.M. (2012) A program for annotating and predicting the effects of single nucleotide polymorphisms, SnpEff: SNPs in the genome of *Drosophila melanogaster* strain w1118; iso-2; iso-3. *Fly*, **6**, 80–92.
71. Xin-Zhao Wang, C., Zhang, K., Aredo, B., Lu, H. and Ufret-Vincenty, R.L. (2012) Novel method for the rapid isolation of RPE cells specifically for RNA extraction and analysis. *Exp. Eye Res.*, **102**, 1–9.
72. Nordgard, O., Kvaloy, J.T., Farmen, R.K. and Heikkila, R. (2006) Error propagation in relative real-time reverse transcription polymerase chain reaction quantification models: the balance between accuracy and precision. *Anal. Biochem.*, **356**, 182–193.
73. Lee, Y., Kameya, S., Cox, G.A., Hsu, J., Hicks, W., Maddatu, T.P., Smith, R.S., Naggert, J.K., Peachey, N.S. and Nishina, P.M. (2005) Ocular abnormalities in *Large*^{myd} and *Large*^{vls} mice, spontaneous models for muscle, eye, and brain diseases. *Mol. Cell. Neurosci.*, **30**, 160–172.
74. Inoue, K., Hara, Y. and Sato, T. (2012) Development of the oxytalan fiber system in the rat molar periodontal ligament evaluated by light- and electron-microscopic analyses. *Anat. Anz.*, **194**, 482–488.
75. Tiedemann, K., Batge, B., Muller, P.K. and Reinhardt, D.P. (2001) Interactions of fibrillin-1 with heparin/heparan sulfate, implications for microfibrillar assembly. *J. Biol. Chem.*, **276**, 36035–36042.
76. Weinbaum, J.S., Broekelmann, T.J., Pierce, R.A., Werneck, C.C., Segade, F., Craft, C.S., Knutsen, R.H. and Mecham, R.P. (2008) Deficiency in microfibril-associated glycoprotein-1 leads to complex phenotypes in multiple organ systems. *J. Biol. Chem.*, **283**, 25533–25543.
77. Trask, B.C., Broekelmann, T., Ritty, T.M., Trask, T.M., Tisdale, C. and Mecham, R.P. (2001) Posttranslational modifications of microfibril associated glycoprotein-1 (MAGP-1). *Biochemistry*, **40**, 4372–4380.
78. Krebs, M.P., White, D.A. and Kaushal, S. (2009) Biphasic photoreceptor degeneration induced by light in a T17 M rhodopsin mouse model of cone bystander damage. *Invest. Ophthalmol. Vis. Sci.*, **50**, 2956–2965.
79. Low, B.E., Krebs, M.P., Joung, J.K., Tsai, S.Q., Nishina, P.M. and Wiles, M.V. (2014) Correction of the *Crb1*^{rd8} allele and retinal phenotype in C57BL/6N mice via TALEN-mediated homology-directed repair. *Invest. Ophthalmol. Vis. Sci.*, **55**, 387–395.

80. Schindelin, J., Arganda-Carreras, I., Frise, E., Kaynig, V., Longair, M., Pietzsch, T., Preibisch, S., Rueden, C., Saalfeld, S., Schmid, B. *et al.* (2012) Fiji: an open-source platform for biological-image analysis. *Nat. Methods*, **9**, 676–682.
81. Forster, B., Van De Ville, D., Berent, J., Sage, D. and Unser, M. (2004) Complex wavelets for extended depth-of-field: a new method for the fusion of multichannel microscopy images. *Microsc. Res. Tech.*, **65**, 33–42.
82. Preibisch, S., Saalfeld, S. and Tomancak, P. (2009) Globally optimal stitching of tiled 3D microscopic image acquisitions. *Bioinformatics*, **25**, 1463–1465.
83. Nair, K.S., Hmani-Aifa, M., Ali, Z., Kearney, A.L., Ben Salem, S., Macalinao, D.G., Cosma, I.M., Bouassida, W., Hakim, B., Benzina, Z. *et al.* (2011) Alteration of the serine protease PRSS56 causes angle-closure glaucoma in mice and posterior microphthalmia in humans and mice. *Nat. Genet.*, **43**, 579–584.